Industrial Chemistry & Materials

ROYAL SOCIETY OF CHEMISTRY

MINI REVIEW

View Article Online
View Journal

Cite this: DOI: 10.1039/d3im00109a

Recent progress in nickel single-atom catalysts for the electroreduction of CO_2 to CO

Ziyan Yang,[a] Rongzhen Chen,[a] Ling Zhang,[a] Yuhang Li *[a] and Chunzhong Li *[b]

Received 14th October 2023,
Accepted 14th December 2023

DOI: 10.1039/d3im00109a

rsc.li/icm

The electrocatalytic reduction of carbon dioxide (CO_2) is considered an effective strategy for mitigating the energy crisis and the greenhouse effect. Nickel is widely used in single-atom catalysts (SACs) owing to its special electronic structure. In this minireview, the basic principles of Ni SACs in the electrocatalytic reduction of CO_2 to CO are first described. Subsequently, Ni SACs are divided into three categories depending on different strategies used to improve properties. The synthesis, morphology, performance and theoretical calculations of the catalysts are also described. Finally, an overview of the existing challenges and perspectives of Ni SACs for CO_2 reduction is presented.

Keywords: CO_2 reduction; Electrocatalysis; Nickel single-atom catalysts.

1 Introduction

Since the industrial revolution of the 18th century, fossil fuel consumption has been rising. Consequently, the emission of CO_2 has also increased drastically. This has led to a number of environmental issues that can no longer be ignored, especially the energy crisis and the greenhouse effect.[1] Some studies have proposed that the atmospheric CO_2 concentration could reach 570 ppm by 2100, which raises awareness of the importance of closing the carbon cycle. The use of clean energy to drive the CO_2 reduction reaction (CO_2-RR) to convert CO_2 into value-added fuels and chemicals is widely considered one of the most promising strategies.[2] For instance, electrocatalysis, photocatalysis and thermocatalysis are the most popular routes nowadays.[3] Electrochemical CO_2 reduction (ECR) aims to transfer CO_2 into chemicals and fuels by generating electricity from renewable energy sources, such as wind, solar and tidal energy. ECR has attracted considerable attention owing to its following advantages: 1) easier access to products such as methanol and C_{2+} compared to thermocatalysis, especially at a low pressure; 2) lower temperature and pressure requirements for the

[a] Key Laboratory for Ultrafine Materials of Ministry of Education, Shanghai Engineering Research Center of Hierarchical Nanomaterials, School of Materials Science and Engineering, East China University of Science and Technology, Shanghai 200237, People's Republic of China. E-mail: yuhangli@ecust.edu.cn
[b] Key Laboratory for Ultrafine Materials of Ministry of Education, Shanghai Engineering Research Center of Hierarchical Nanomaterials, School of Chemical Engineering, East China University of Science and Technology, Shanghai 200237, People's Republic of China

Ziyan Yang

Ziyan Yang received her Bachelor's degree in Polymer Materials Science and Engineering from the East China University of Science and Technology in 2022. She is pursuing her master's degree in Materials Science and Engineering at the East China University of Science and Technology under the supervision of Prof Ling Zhang and Yuhang Li. Her current research interests focus on the design and synthesis of novel electrocatalysts for the CO_2 reduction reaction.

Yuhang Li

Yuhang Li received his B.S. (2011) and Ph.D. (2016) degrees from ECUST. He worked at the Key Laboratory for Ultrafine Materials of Ministry of Education as a postdoctoral fellow from 2016 to 2018 at ECUST. He visited the University of Toronto as a visiting fellow in 2019–2021. He is currently an associate professor at the School of Materials Science and Engineering, ECUST. His research interest focuses on the design and synthesis of functional coordination electrocatalytic materials and electro-synthetic processes.

reaction process, resulting in a gentler reaction environment; 3) modular reaction systems have more potential to be scaled up for industrial applications; 4) more environmentally friendly using renewable energy resources, such as solar and wind, to drive CO_2RR.[4,5] However, ECR still faces challenges with product separation, unavoidable competitive hydrogen evolution reaction (HER), sluggish kinetics, and inert thermodynamics.

ECR produces an extensive variety of products, the most typical of which are CO, CH_4, HCOOH, CH_3OH, CH_3CH_2OH, HCHO, and C_2H_4. Note that CO_2RR is unavoidably accompanied by HER, and therefore, the products always contain hydrogen. Up to now, metal oxides, metal alloys, metal nanoparticles and composite materials have undergone broad investigation.[6–12] In addition, the electronic structures of catalysts have a considerable influence on the contribution of products.[13,14] SACs have prompted high research interest owing to their maximum atom-utilization efficiency, adjustable coordination structures and tunable catalytic properties.[15,16] Hence, the application of SACs in CO_2RR could effectively control the distribution of products and alleviate the cost of product separation.

Among the multiple reduction products, CO is regarded as having the highest market value as it is a crucial feedstock for the Fischer–Tropsch process, which can synthesize high-value long-chain hydrocarbons.[17] Moreover, because CO is a gaseous product, the complicated and expensive post-treatment procedure of gas–liquid separation is avoided. In recent years, transition metals (Fe, Co and Ni) with unique electronic structures and abundant sources have attracted a lot of attention. Although these metals are designed to be dispersed at the atomic level, the catalysts show impressively high selectivity for CO in ECR. In particular, Ni SACs always exhibit superior performance. However, the reaction mechanism remains unclear. In some studies, DFT calculations based on crystal-field theory indicate that the d-orbital electronic configurations of central metals are significant to the selectivity and activity of CO_2RR.[18,19] The central Ni atoms of the Ni SACs are more likely to form the vacant outermost d-orbital that facilitates electron transfer between the C atom of CO_2 and the Ni atom. Consequently, CO_2 molecules adsorbed on the catalyst surface can be efficiently activated. Ni SACs can also minimize the reaction potential of CO_2–CO conversion, which enhances the selectivity towards CO.

This review begins by introducing the reaction pathway of CO_2RR to generate CO. Then, it describes the current methods and mechanisms for identifying the active sites of Ni SACs. Subsequently, the recently developed nickel-based nitrogen-doped carbon single-atom catalytic materials are divided into the following three categories based on the different strategies used to boost catalytic performance: 1) different structures of supports, 2) coordination structure regulation, and 3) surface modification. Finally, we summarize the existing challenges of Ni SACs and provide an outlook on future development.

2 Fundamental mechanisms

2.1 Reaction pathway

Experimental research and theoretical simulation show that the whole CO_2RR progress can be divided into three parts: 1) CO_2 molecules adsorbed on the catalyst surface; 2) multiple proton-coupled electron transfer (PCET) processes occur between the catalyst and the absorbed CO_2 to activate linear CO_2 molecules and form key intermediates; and 3) product desorption from the surface of the catalysts. The PCET process is an essential part of the entire reaction that determines the type of target products. However, some studies have indicated that the activation of CO_2 is associated only with electron transfer and without proton coupled.[16] Thus far, the experimental products of CO_2RR mainly include CO, HCOOH, CH_3OH, CH_4, C_2H_4 and C_2H_5OH. The corresponding half reactions and equilibrium potentials (*versus* reversible hydrogen electrode (RHE)) are listed as follows (Table 1):[20]

CO_2RR is normally accompanied by inert thermodynamics and sluggish kinetics, which is associated with the high dissociation energy of the C═O bond in CO_2 and the multiple PCET steps.[21] Therefore, electrocatalysts are essential for CO_2RR processes, which are the most promising to accelerate the reaction rates, lower the overpotential, and even improve the selectivity. Among the various electrocatalysts, such as metal–organic complexes, metal alloys, and metal oxides, single-atom catalysts display superior catalytic performance. Numerous experimental results have shown that the main product of CO_2-RR on SACs is CO. The mechanism of the electrochemical conversion of CO_2 to CO at single-atom sites typically involves the following steps:

$$CO_2 + * \rightarrow *CO_2 \quad (1)$$

$$*CO_2 + H^+ + e^- \rightarrow *COOH \quad (2a)$$

$$*CO_2 + e^- \rightarrow *CO_2^{\bullet -} \quad (2b)$$

$$*CO_2^{\bullet -} + H^+ \rightarrow *COOH \quad (2c)$$

Chunzhong Li

Chunzhong Li received his B.S. (1989), M.S. (1992), and Ph.D. (1997) degrees from ECUST. He became a full professor at the School of Materials Science and Engineering, ECUST in 1998, and now he is the dean of the School of Chemical Engineering, ECUST. His research interest includes nanomaterials chemical engineering and low-carbon energy chemical engineering.

Table 1 Electrochemical reactions with equilibrium potentials

Reaction	E_0 (V *vs.* RHE)	(Product) name
$CO_2 + 2H^+ + 2e^- \rightarrow CO + H_2O$	−0.10	Carbon monoxide
$CO_2 + 2H^+ + 2e^- \rightarrow HCOOH$	−0.12	Formic acid
$CO_2 + 6H^+ + 6e^- \rightarrow CH_3OH + H_2O$	0.03	Methanol, MeOH
$CO_2 + 8H^+ + 8e^- \rightarrow CH_4 + 2H_2O$	0.17	Methane
$2CO_2 + 12H^+ + 12e^- \rightarrow C_2H_4 + 4H_2O$	0.08	Ethylene
$2CO_2 + 12H^+ + 12e^- \rightarrow C_2H_5OH + 3H_2O$	0.09	Ethanol, EtOH

$$*COOH + H^+ + e^- \rightarrow *CO + H_2O \quad (3)$$

$$*CO \rightarrow CO + *, \quad (4)$$

where * denotes the active sites on the catalyst surface.

First, the C atom of the CO_2 molecule is absorbed on the active site of the SACs (eqn (1)). In the next process, *COOH is widely believed to be the key intermediate for the reduction of CO_2 to CO. However, two paths possibly form *COOH. One is through a single PCET process (eqn (2a)), and the other is through a single electron transfer to convert $*CO_2^{\bullet-}$ intermediate (eqn (2b)), which then quickly gains a proton to form *COOH (eqn (2c)).[22,23] But if the binding between the C atom and the active site is not strong enough, free $CO_2^{\bullet-}$ intermediate potential forms HCOOH through an out-sphere reaction pathway.[24] Then, the *COOH intermediate undergoes proton electron transfer and subsequently forms the *CO intermediate (eqn (3)). Finally, *CO desorbs from the active sites and indicates the accomplishment of reducing CO_2 to CO (eqn (4)). The whole corresponding process is regarded as a proton-decoupled electron transfer mechanism (PDET).

2.2 Active sites

In recent studies, SACs have shown great advantages in enhancing activity, selectivity, and stability. Many experimental studies have demonstrated that SACs combine the properties of both homogeneous and heterogeneous electrocatalysts.[25] It is generally agreed that SACs downsize the active sites to an atomic scale and therefore obtain extraordinary electronic structure, powerful metal–support interactions, low-coordinated metal atoms, and maximum atom utilization simultaneously. However, it remains a great challenge to investigate the source of these excellent properties and reveal the mechanism that is essential for precisely regulating the performance of CO_2RR.

Among single-atom catalysts, metal and nitrogen doped carbon (M–N–C) catalysts have been widely explored. The single atom sites with nitrogen coordinated (M–N_x) in M–N–Cs are assumed to be significantly different from corresponding metal counterparts in molecular and electronic structures, enabling them to be more active in key catalytic reactions.[26] Early in the study, the Fe–N–C system shows excellent performance for oxygen reduction reaction (ORR) in both acidic and alkaline media. The atomically dispersed Fe–N_x sites have been convincingly proved to be active for ORR through several physical characterization techniques and catalytic tests, with Fe–N_4 being a particularly potential structure of active sites.[27–29] As Ni–N–C catalysts display a significant promise in CO_2RR, more and more researchers have been studying whether Ni–N_x is the source of its activity.

The first challenge is to prove the single atomic site and characterize the coordinated structure of metal atoms. Koshy *et al.*[30] combined single-atom electron energy loss spectroscopy (EELS), annular dark-field scanning transmission electron microscopy (ADF-STEM), and time-of-flight secondary ion mass spectrometry (ToF-SIMS) to show conclusive proof of the presence of NiN_x. They prepared three NiPACN samples with different Ni loadings: NiPACN-0.5 wt% Ni, NiPACN-3.5 wt%, and PR-NiPACN-3.5 wt% (postreaction high Ni loading NiPACN sample). The ADF-STEM images showed that Ni atoms were dispersed atomically and even remained after exposure to electrochemical CO_2RR. Then, atomic resolution EELS is applied to NiPACN-3.5 wt%, which shows the coexistence of N K-edge and Ni L-edge signals on single Ni atoms and affords microscopic evidence for NiN_x coordination. Finally, the results of the ToF-SIMS showed the presence of NiN_xC_y fragments, thereby directly confirming the coordination of the single Ni atom with nitrogen. With the comparison of Ni phthalocyanine, the active sites are supposed to be NiN_4.

The second challenge is to correlate the NiN_x sites with electrochemical activity. Koshy and his co-workers[31] have investigated this through hard and soft X-ray spectroscopy. The NiN_x sites are most likely to be the active sites for reducing CO_2 into CO after comparing with Ni aggregates. Then, three NiPACN samples with different Ni loadings of 0 wt%, 0.5 wt% and 3.4 wt% were prepared. Moreover, as the Ni loading increases, the partial current density of CO (j_{CO}) also increases until the STEM-HAADF and XRD have observed the appearance of Ni nanoparticles (NPs) in the catalyst. The hard and soft X-ray spectroscopic results reveal that pyrrolic-coordinated Ni atoms are active sites that strongly resemble the active sites of molecular Ni porphyrin catalysts.

The highly heterogeneous nature of Ni–N–C leads to difficulty in characterization by nonspatially resolved methods. Zhang *et al.*[32] have found that scanning transmission X-ray microscopy (STXM) is an effective tool for exploring this catalyst. The results also reveal that NiN_x is the source of high activity. Up to now, most studies have identified active sites by comparing different metal loading samples with *ex situ* characterization methods. It remains a

Table 2 Performance of Ni SAC electroreduction of CO_2 to CO

Electrocatalysts	Reactors	Electrolyte	$FE_{CO\ max}$ (%)	Potential (*vs.* RHE)	Total current density (mA cm^{-2})	TOF (h^{-1})	Ref.
Ni–N–C	H cell	0.5 M $KHCO_3$	97	−0.65	15	3200	18
Ni-N-Gr	A separated electrochemical cell	0.1 M $KHCO_3$	~95	−0.7	>0.2	2700	35
Ni-NG	Membrane electrode assembly (MEA)	0.1 M $KHCO_3$	97	2.78 V (cell voltage)	50	210 000	36
Ni-NG-acid	H cell	0.5 M $KHCO_3$	97	−0.9	27.2	2278	37
Ni@NCNTs	H cell	0.5 M $KHCO_3$	99.1	−0.8	8.08	—	38
NiSA-N-CNTs	A gas-tight electrochemical cell	0.5 M $KHCO_3$	91.3	−0.7	25.7	90 000	39
A-Ni@CMK	Flow cell	1 M KOH	99.5	−0.6	248	—	40
Ni-NC(AHP)	H cell	0.5 M $KHCO_3$	~100	−0.9	14.5	7500	41
Ni-NC(HPU)	H cell	0.5 M $KHCO_3$	91	−0.8	27.1	3250	42
NiSA-NGA-900	H cell	0.5 M $KHCO_3$	90.2	−0.8	6.5	—	43
Ni-HPNCFs	H cell	0.5 M $KHCO_3$	97	−1.0	59.6	24 900	44
Ni–N–C-900	Flow cell	1 M KOH	98	−0.96	400	>5500	45
SA-NiNG-NV	H cell	0.5 M $KHCO_3$	96.4	−0.7	12.5	1000	46
NiNG-S	H cell	0.5 M $KHCO_3$	97	−0.8	22.5	2000	47
Ni–N_4–O/C	H cell	0.5 M $KHCO_3$	99.2	−0.9	23.2	11 187	48
NiSA(0.3)-N-PGC	H cell	0.1 M $KHCO_3$	97.2	−0.76	25	7000	49
Ni/Fe–N–C	H cell	0.5 M $KHCO_3$	98	−0.7	9.5	3000	50
Ni/Cu–N–C	H cell	0.5 M $KHCO_3$	97.7	−0.7	14.0	7000	51
Ni-N_3-NCNFs	Flow cell	1 M $KHCO_3$	96	−0.72	150	—	52
Ni@C_3N_4-CN	H cell	0.5 M $KHCO_3$	~99	−0.8	4	2000	53
$Ni_{0.037}$-NG-H	H cell	0.5 M $KHCO_3$	97.3	−0.8	15.4	—	54
Ni@N-C	Flow cell	1 M KOH	97	−1.1	244	—	55
Ni(NC)	Flow cell	1 M KOH	99	−1.82	160	—	56
Ni_{NP2}@Ni_{SA2}-NG	Flow cell	1 M KOH	98	−0.58	200	—	57
NiO/Ni–N–C-800	H cell	0.1 M $KHCO_3$	96.5	−1.1	16.5	9200	58

big challenge to develop *in situ* and *operando* technologies to directly observe the involvement of NiN_x sites in the reaction and understand the mechanisms of the CO_2RR.[33]

3 Classification of Ni SACs

In recent years, Ni SACs have been extensively researched because of the high selectivity of CO and the inhibition of competing hydrogen evolution reactions (HER).[34] Table 2 displays some of the reported Ni SACs for the conversion of CO_2 to CO and superior performance. As shown in Fig. 1, based on different strategies to enhance performance, Ni SACs can be classified into the following three kinds: (1) different structures of supports, (2) coordination structure regulation, and (3) surface modification.

3.1 Different structures of supports

The traditional structure of Ni SACs is that the central nickel atom is uniformly distributed on supports and is in coordination with four nitrogen atoms (Ni–N_4). Carbon supports allow fast electron transport and have advantages in terms of high electrical conductivity. In addition, these supports show low activity toward the competing HER.[59] With all these unique properties, carbon frameworks are extensively exploited for bonding single atom sites. The most popular types are carbon nanotubes, graphene, and carbon black.

3.1.1 Graphene and derivatives. The most typical method for synthesizing SACs is pyrolysis, which requires heating the precursors at high temperatures for several hours. However, Ni–N bonds break very susceptibly when heated at high temperatures. Therefore, when Fe SACs and Co SACs are explored extensively, no studies related to Ni SACs have been reported initially. Until 2016, Su *et al.*[35] successfully applied a thermal treatment strategy in metal complexes with graphene oxide to synthesize Ni SACs. They first prepared graphite oxides (GOs) and Ni-pentaethylenehexamine (Ni-PEHA) complexes. Then, GOs and Ni-PEHA were mixed with ethanol.

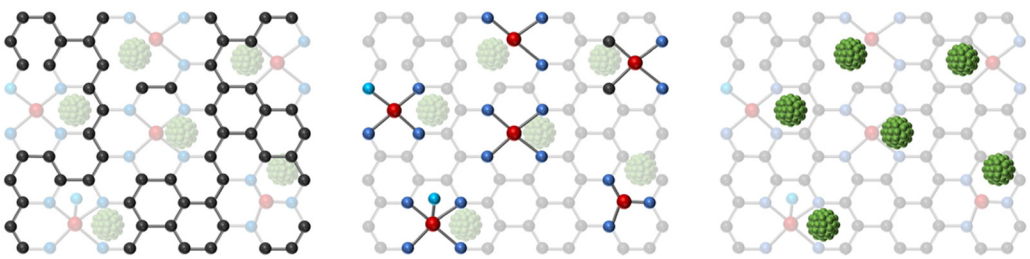

Fig. 1 Schematic representation of the classification of Ni SACs according to different regulatory strategies.

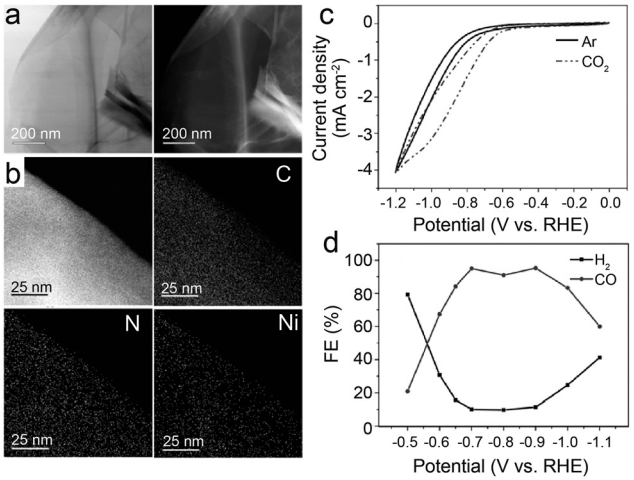

Fig. 2 (a) Representative TEM image of Ni-N-Gr (left) and corresponding high-angle annular dark-field scanning image (right). (b) High-resolution TEM image of Ni-N-Gr and corresponding EDX maps of C, N, and Ni. (c) Cyclic voltammograms of Ni-N-Gr catalyst in CO_2-saturated 0.1 M $KHCO_3$ and Ar-saturated 0.1 M KH_2PO_4/K_2HPO_4 (pH = 6.8) at 10 mV s^{-1}. (d) FEs for the reduction products generated by Ni-N-Gr catalyst.[35] Reprinted with permission from Wiley-VCH, copyright 2016.

After drying the homogeneous mixture, it was laid at the bottom of an Ar-filled quartz tube. The tube was quickly placed in the muffle furnace for 45 seconds at 900 °C and immediately cooled to ambient temperature in a protective atmosphere of argon. Finally, the graphene was washed by H_2SO_4, and eventually Ni–N-doped graphene (Ni-N-Gr) was obtained. High-resolution transmission electron microscopy (HR-TEM) obviously demonstrates the absence of nanoparticles (Fig. 2a). The corresponding energy-dispersive X-ray (EDX) elemental maps show that the N and Ni atoms uniformly disperse on the graphene sheets (Fig. 2b). The absence of peaks associated with Ni in XRD further proves the existence of nanoparticles. The results of X-ray photoelectron spectroscopy (XPS) and extended X-ray absorption fine structure (EXAFS) are consistent with the generation of a single Ni atom and the incorporation of the Ni–N coordination structure into the graphene substrate. In the electrochemical performance tests, Ni-N-Gr shows electrocatalytic CO_2 reduction activity with a −0.5 V *versus* reversible hydrogen electrode (RHE) onset potential in CO_2-saturated solution (Fig. 2c). The main product is CO, and the sample shows the highest activity with a faradaic efficiency (FE) of more than 90% at −0.7 to −0.9 V (Fig. 2d). The FE of H_2 further increases at more negative potentials, meaning that the HER came to dominate. Finally, the electro-catalytic stability of Ni-N-Gr was measured at −0.65 V *versus* RHE (the potentials are all *versus* RHE unless otherwise specified) for 5 h in a $KHCO_3$ solution saturated with CO_2.

Graphene, as a two-dimensional layered material, has various chemical coordination environments and well-defined atomic structures that modulate the electronic properties of confined intra-layer guest atoms. Thus, if individual atoms are controllably confined in graphene vacancies, the nickel electronic structure can be efficiently tuned to achieve selective CO_2–CO conversion. Jiang *et al.*[36] scattered single Ni atoms into a layered graphene nanosheet (NS), denoted as Ni-NG. The atomic dispersion and atomic coordination of Ni have been confirmed by *operando* X-ray absorption spectroscopy (XAS) and aberration-corrected scanning transmission electron microscopy (STEM). The XANES and EXAFS of Ni and N in Ni-NG are only slightly different from those of Ni-Pc, suggesting that Ni–N_4 is the dominant structure. The catalytic activity for CO_2RR was tested by drop-casting onto a mirror-polished glassy carbon electrode and then set into a standard three-electrode H-cell configuration with an electrolyte of CO_2-saturated 0.5 M $KHCO_3$. The onset potential is −0.31 V; the FE of CO rises quickly to 83% at −0.60 V, and it is maintained above 90% until −0.87 V. After increasing the catalyst loading to 1 mg cm^{-2} by changing the electrode to carbon fiber paper, the current density increases drastically. At a 620 mV overpotential, CO FE reached a maximum of about 95% at a current density of around 11 mA cm^{-2}. The current density did not increase linearly as the catalyst loading increases probably owing to the overlapping graphene layers on the carbon fiber paper. In addition, after over 20 hours of continuous measurement, Ni-NG maintains a stable current density with a CO selectivity of about 90%, which represents impressive electrocatalytic durability. Wang *et al.*[37] also found that the annealing temperature during the synthesis of the catalyst is essential to tuning both the properties of the graphene layer and the distribution of the single nickel sites. They synthesized the catalysts at four temperatures (700, 800, 900, and 1100 °C) and then processed them in 0.5 M H_2SO_4 for acid treatment. The products are denoted as Ni-NG-*X*-acid (where *X* represents the temperature). Images of TEM suggest that higher reaction temperatures are conducive to C–N cleavages, leading to more defects in graphene layers for Ni NPs to transport and generate larger particles without fully enveloping the graphene shell. Hence, after annealing and acid treatment, the catalyst embeds more active Ni sites in hollow graphene shells. In combination with XRD patterns, Raman spectra, and TEM, all the outstanding performance is attributed to the greater specific surface area owing to a higher degree of graphitization at higher temperatures, allowing for more exposure of the Ni active sites. Electrochemical performance tests indicate that 1000 °C is the optimum annealing temperature. Within a wide potential window of −0.7 V to −1.2 V, the CO FE is above 90%. At −1.2 V, j_{CO} achieves 27.2 mA cm^{-2}.

3.1.2 Mesoporous carbon and derivatives. Zheng *et al.*[38] revealed that the confinement effect of N-doped carbon nanotubes (NCNTs) can facilitate *CO desorption by lowering the binding strength between *CO intermediates and Ni NPs. Besides, SACs with CNT as the substrate material usually show excellent stability in CO_2RR. Such a curved surface has been proven to have more extraordinary catalytic activity owing to a lower energy barrier to form the key intermediate and higher total density of states around the Fermi level.[60]

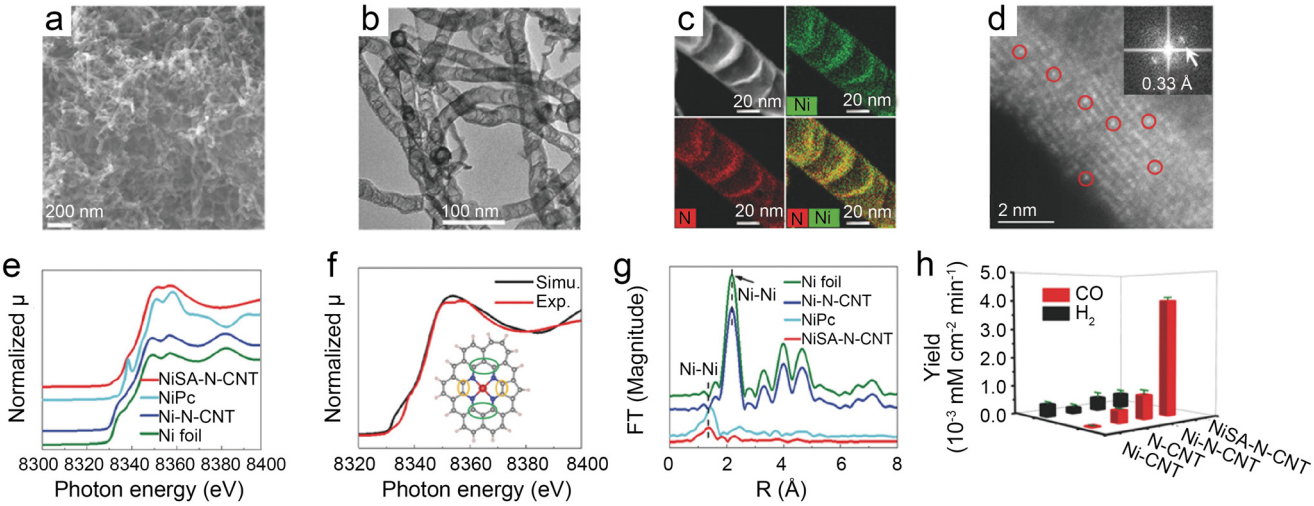

Fig. 3 (a–d) Characterization of NiSA-N-CNTs, (a) scanning electron microscopy (SEM) image; (b) transmission electron microscopy (TEM) image; (c) STEM-EDS mapping; (d) ADF image showing the Ni single atoms located on the walls of a CNT (the red circles show typical Ni atoms embedded in the carbon plane of walls. The insert is the Fourier transform of (d)); (e–g) chemical environment of NiSA-N-CNTs as probed *via* X-ray absorption spectroscopy; (e) Ni K-edge spectra of the EXAFS spectrum; (f) comparison of a simulated XANES spectrum of the inserted Ni-core structure with experimental results; (g) Fourier transform of the EXAFS spectrum of Ni foil, Ni-N-CNTs, NiPc, and NiSA-N-CNTs; and (h) product yields of NiSA-N-CNTs, Ni-N-CNTs, N-CNTs, and Ni-CNTs for CO_2RR at −0.55 V.[39] Reprinted with permission from Wiley-VCH, copyright 2018.

Cheng *et al.*[39] used a new multi-step pyrolysis process to synthesize a SAC with a high metal loading of 20 wt%, which is based on atomically dispersed Ni on NCTs (NiSA-N-CNTs). From SEM and TEM, no Ni NPs are observed (Fig. 3a and b). The atomic dispersion of Ni in NiSA-N-CNTs is displayed in STEM-EDS mappings and AC-STEM-ADF images (Fig. 3c and d). The absence of a pre-edge signature at 8338 eV in the EXAFS of the NiSA-N-CNT indicates that the structure of Ni–N is not planar (Fig. 3e). Through the combination of STEM images and first-principle simulation of the XANES, this work establishes the coordination structure of the Ni atom with two carbon shells following the four nearest N-coordination shells (Fig. 3f). Based on the model, the fitting result suggests that Ni is in the configuration of Ni–N_4, which is similar to the coordination of Ni in NiPc (Fig. 3g). In the multistep pyrolysis process, Ni single atoms were limited by the cavity, thus inhibiting aggregation and forming NiSA-N-CNTs with Ni–N_4 structure. For NiSA-N-CNTs, CO and H_2 are the only products for the CO_2RR. At −0.55 V, the CO yield is up to 4.00×10^{-3} mmol cm^{-2} min^{-1} while that of H_2 is significantly lower (Fig. 3h). At this point, the FE CO increases to 89.0%, and as the voltage becomes more negative until −0.70 V, the FE CO reaches a maximum of 91.3%. After 12 hours of electrolysis, there is still no significant aggregation and demetallation of the atomically dispersed Ni.

Ni SACs always have quite a low onset potential that represents high intrinsic activity. Thus, regulating the morphological configuration to increase the number of exposure active sites is considered an effective strategy to increase the CO_2RR kinetics on Ni SACs. Chen *et al.*[40] developed a superior Ni SAC with mesoporous carbon denoted as A-Ni@CMK by a step-by-step pore-filling synthetic strategy (Fig. 4a). Relative experimental studies along with density functional theory (DFT) calculations indicate that the higher density active Ni–N_4 sites, uniform mesoporous channels and the large surface area of the carbon support enhance the reaction kinetics. The A-Ni@CMK displays superior performance in the H-cell with a CO FE of over 80% in a wide electrochemical potential window of −0.5 to −0.9 V (Fig. 4b). The j_{CO} reaches 51 mA cm^{-2} at −0.8 V (Fig. 4c). In the flow cell, the FE CO is more than 95% at −0.8 V with an industrial-level j_{CO} value of 366 mA cm^{-2} (Fig. 4d).

3.1.3 Others. The hollow structure is assumed to facilitate the transport of key intermediates. Li *et al.*[41] constructed assembled hollow plates (AHP) of N-rich carbon for loading the single Ni atom to synthesize a high-efficiency catalyst (denoted as Ni-NC(AHP)) using a dual-linker zeolitic tetrazolate framework-engaged method (Fig. 5a). These microspheres assembled from nanoplates (Fig. 5b) also have greater mesoporosity and a larger surface area, which can promote mass transport and provide more exposed single Ni sites. The linear sweep voltammetry (LSV) curves obtained from the measurement in the H-cell indicate an onset potential of −0.6 V (Fig. 5c). In particular, an FE CO of approximately 100% is achieved over a wide potential window ranging from −0.7 to −1.0 V (Fig. 5d). Moreover, the small Tafel slope (101 mV dec^{-1}) of the Ni-NC(AHP) catalyst proves that the special structure provides faster kinetics (Fig. 5e).

To further design catalysts with favorable mass transfer and highly accessible discrete active sites, Li *et al.*[42] developed a credible Ni-templated and Ni-catalyzed method for converting metallic Ni into single-Ni atoms anchored on hollow porous urchin-like N-doped carbon to synthesize a superior SAC (denoted as Ni-NC(HPU)) (Fig. 6a). The distinctive hollow thorns on the surface (Fig. 6b and c)

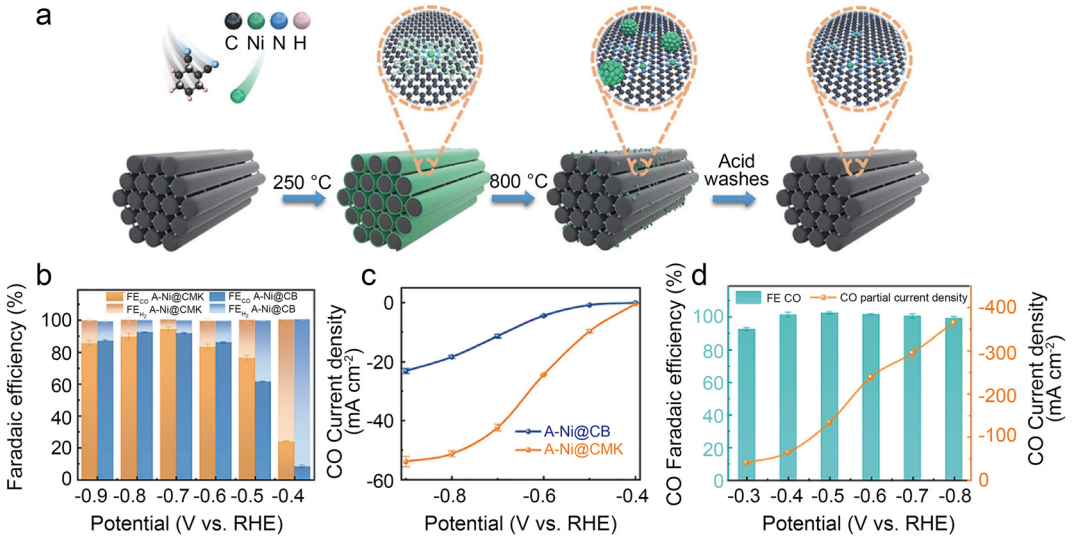

Fig. 4 (a) Schematic illustration of the synthesis of A-Ni@CMK; (b) FE_{CO} and FE_{H_2} of A-Ni@CMK and A-Ni@CB in the H-type cell; (c) j_{CO} of A-Ni@CMK and A-Ni@CB in the H-type cell; and (d) electrocatalytic activity of A-Ni@CMK in the flow cell.[40] Reprinted with permission from Wiley-VCH, copyright 2021.

contribute to a large external surface area and excellent conductivity, increasing the exposure of single-Ni sites and accelerating mass transfer, especially electron transfer. Meanwhile, this unusual shape does not affect the uniform atomic dispersion of Ni (Fig. 6d). The results of the examination of the H-type cells indicate that the main products are CO and H_2. The FE of CO reaches 91% with a j_{CO} of 24.7 mA cm^{-2} when operated at −0.8 V. Furthermore, in potentials ranging from −0.7 V to −0.9 V, the FE of CO remains above 83% (Fig. 6e and f). The high crystallinity of Ni-NC(HPU) results in good conductivity;[61] thus, this material displays the lowest charge transfer resistance in the electrochemical impedance spectroscopy (EIS) test (Fig. 6g). This work provides new inspiration for synthesizing advanced

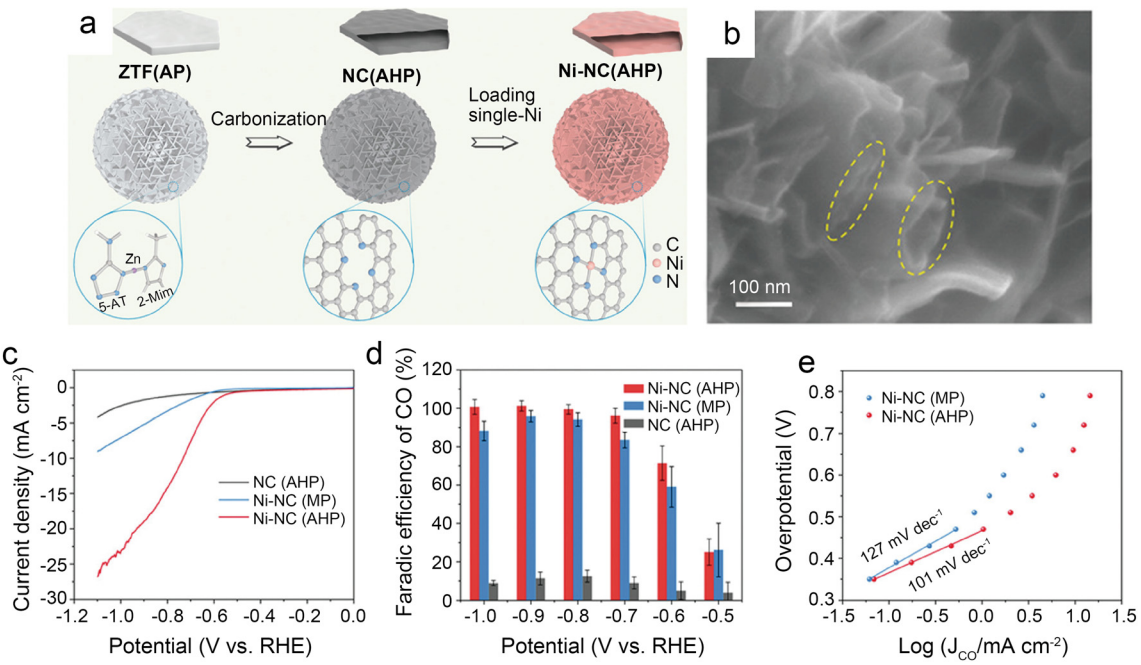

Fig. 5 (a) Schematic illustration of the preparation route for Ni-NC(AHP); (b) FESEM images of Ni-NC(AHP); the dash circles indicate the openings and parallel walls of hollow plates; (c–e) CO_2 electroreduction performance of samples; (c) LSV curves in CO_2-saturated 0.5 M $KHCO_3$ solution; (d) comparison of CO faradaic efficiency at various potentials; and (e) Tafel plots towards CO product.[41] Reprinted with permission from Wiley-VCH, copyright 2021.

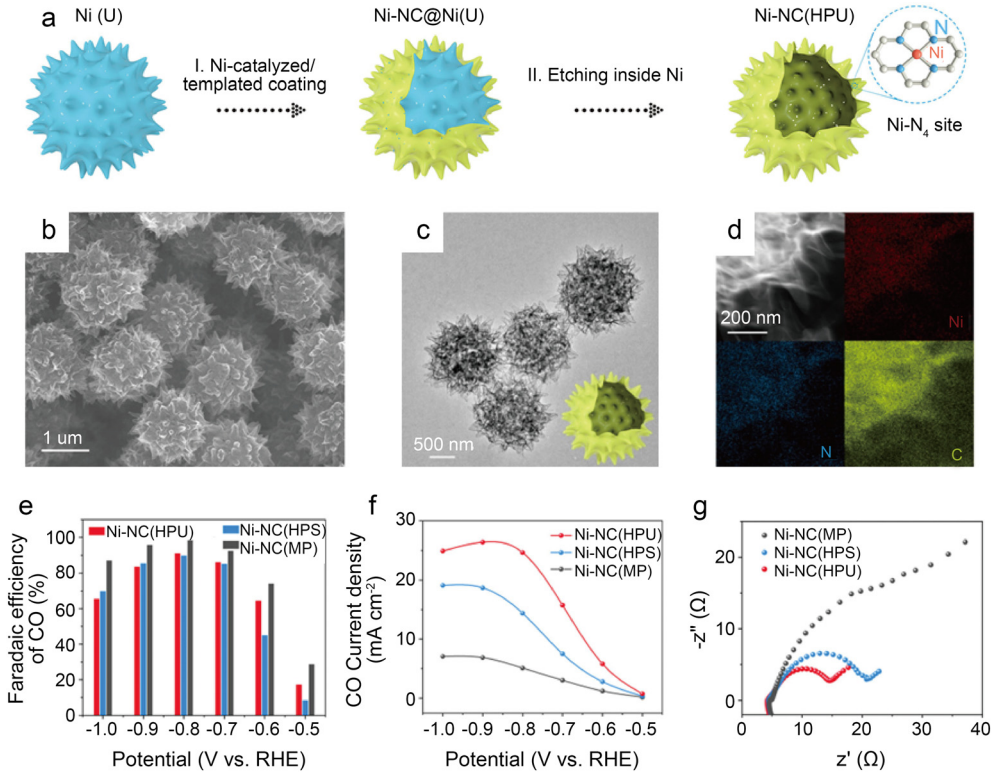

Fig. 6 (a) Schematic illustration of the preparation strategy for Ni-NC(HPU); (b–d) electron microscopy characterizations of Ni-NC(HPU), (b) FESEM images; (c) low-magnification TEM image; (d) dark-field TEM image and EDX elemental mapping images; (e–g) CO_2 electroreduction performance of samples; (e) comparison of CO FE of three samples at various potentials; (f) comparison of CO partial current density at various potentials; and (g) EIS plots obtained at −0.7 V *vs.* RHE.[42] Reprinted with permission from Wiley-VCH, copyright 2022.

single-atom catalysts with hollow porous structures for various energy storage and conversion applications.

3.2 Coordination structure regulation

Because CO_2RR contains multiple PCET processes and the single atom centers of SACs are regarded as active sites, the coordination structures of the metal atomic centers are of particular importance to the electrocatalytic reaction. The typical Ni–N_4 coordination structure with symmetric D_{4h} square-planar geometry is unfavorable for electron transfer. Hence, breaking this symmetry is the key to enhancing CO_2-RR kinetics.[62] The common strategies include tuning coordination numbers, creating vacancies, and diversifying coordination atom species.

3.2.1 Tuning coordination numbers. Nitrogen-doped carbon is the most common substrate used to stabilize metal sites. In general, nitrogen atoms anchor central metal atoms by coordinating with them. Thus, tuning the nitrogen coordination numbers is meaningful in regulating the electronic structure of the active site, which may influence both the adsorption behavior of key intermediates and catalytic performance. Mou *et al.*[43] reported an efficient and simple impregnation–pyrolysis process to synthesize Ni SACs, as shown in Fig. 7a. SEM images and HR-TEM images confirm the absence of Ni nanoparticles on the synthetic catalyst (NiSA-NGA). High-angle annular dark-field scanning transmission electron microscopy (HAADF-STEM) images, STEM images and the relevant EDS elemental mappings of NiSA-NGA clearly illustrate that Ni atoms are atomically dispersed (Fig. 7b and c). The Fourier-transformed EXAFS strongly supports the existence of Ni–N coordination. However, unlike the previously discussed catalysts, the lower relative intensity in NiSA-NGA compared to NiPc implies the unsaturated coordination of Ni atoms (Fig. 7d). The sample obtained by pyrolysis at 900 °C (NiSA-NGA-900) shows the best properties (Fig. 7e–g). At −0.8 V, NiSA-NGA-900 achieves the highest CO FE of 90.2%, corresponding to a current density of around 6 mA cm^{-2}. Considering the origin of excellent behavior, graphene-based aerogels (GA) have a large specific surface area to improve the density of Ni atoms. The DFT calculation shows that the key intermediates (*COOH) can be formed at lower free energies on Ni–N sites with unsaturated coordination compared to Ni–N_4 sites. Besides, ΔG*COOH is much smaller than ΔG*H on Ni–N_2 sites, which inhibits HER and improves the selectivity of CO_2RR. Song *et al.*[44] developed a hard-template method (Fig. 8a) to synthesize high-density Ni–N_x sites with different coordination numbers anchored on the surface of hierarchically porous nitrogen-doped carbon nanofibers (Ni-HPNCFs). The porous HPNCFs have abundant N-doped sites and a large surface area, facilitating the homogeneous dispersion of Ni single atoms. Furthermore, the porous structure of these nanofibers benefits mass transfer and active site exposure. The

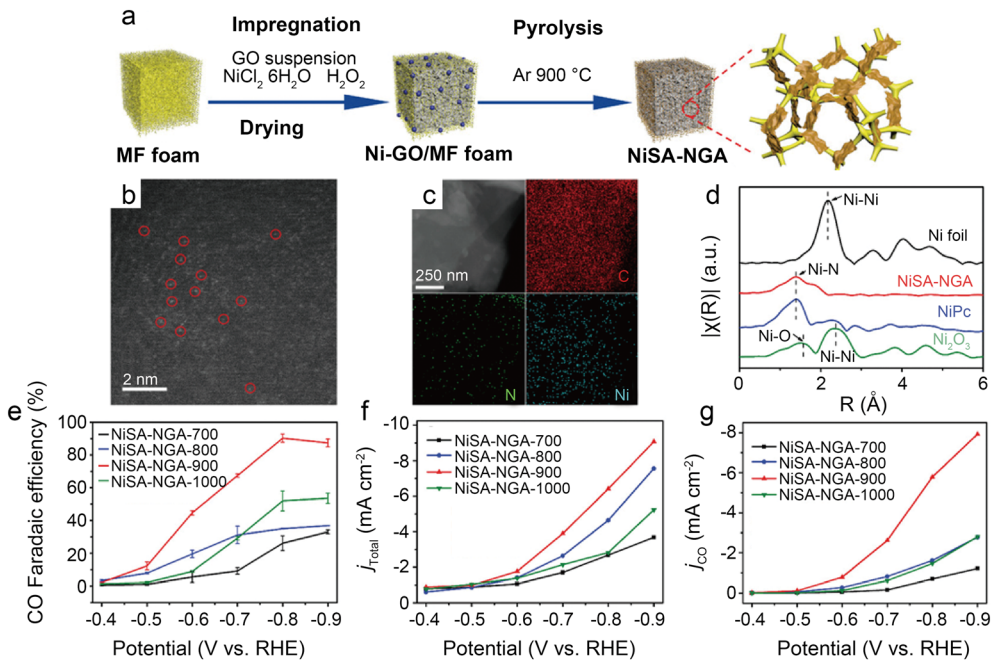

Fig. 7 (a) Schematic illustration of the synthesis of NiSA-NGA; (b) HAADF-STEM image of NiSA-NGA; (c) STEM images and the corresponding energy-dispersive X-ray spectroscopy (EDS) elemental maps of C, N, and Ni for NiSA-NGA; (d) Fourier transformed EXAFS spectra of the Ni K-edge for Ni foil, NiSA-NGA, NiPc, and Ni_2O_3; (e) CO faradaic efficiency; (f) total current density; and (g) partial CO current density of NiSA-NGA catalysts *versus* electrolytic potentials.[43] Reprinted with permission from Wiley-VCH, copyright 2019.

N 1s XPS spectra suppose that the pyrrolic and pyridinic N sites are more likely to anchor Ni atoms than graphitic N, which is further improved by the DFT calculation. By fitting the EXAFS curves, the results show that an average of 2.9 ± 0.1 N atoms is coordinated to the central Ni atom in the sample. In combination with the FT-EXAFS spectra, the Ni–N distance is slightly shorter than that in the $Ni–N_4$ in the porphyrin and phthalocyanine, further demonstrating the formation of the $Ni–N_3$ sites. DFT calculations show that the pyrrole-NiN_3 site plays an important role in inhibiting the formation of H* intermediates for HER. More importantly, it can also reduce the free energies of COOH* generation and CO* desorption. At −0.7 V, the Ni-HPNCF reaches a high CO FE of 97% and a high j_{CO} of 49.6 mA cm^{-2}. This research presents a new approach for adjusting the geometric structure and coordination environment at one time, offering novel inspirations for the future design of higher-performance catalysts.

To accurately control the coordination environment and number of Ni atoms, Li *et al.*[45] explored a unique two-step method (Fig. 8b). In the first step, the particle size range of the ZIF-8 nanocrystal precursors was controlled by adjusting the concentration of zinc salt during the synthesis of ZIF-8. Through one-step carbonization, the precursors were retained in the derived carbon host. This step can produce nitrogen-doped carbon hosts with controlled morphology. In the second step, before thermal activation at relevant temperatures (400 °C, 900 °C, and 1200 °C) to form controlled Ni–N bonds, the Ni ions were introduced in the N-doped carbon host by chemisorption. The thermal activation temperature is vital to control the structure of Ni–N bonds in this method. HAADF-STEM and the corresponding EDS elemental mappings clearly demonstrate that Ni clusters gradually transform into atomically dispersed Ni sites at higher temperatures (Fig. 8c–e). Furthermore, the XAS reveals that Ni–N bonds become shorter at elevated thermal activation temperatures, which is associated with structural distortion in graphene. Besides, XPS indicates that Ni–N–C-1200 samples have less total and pyridinic nitrogen content than Ni–N–C-900, which can be attributed to higher temperatures, resulting in the loss of N atoms and favoring the formation of the $Ni–N_3$ structure. Based on the EXAFS fitting, the Ni–N coordination number of Ni–N–C-1200 is 3.54, suggesting the coexistence of $Ni–N_3$ sites and $Ni–N_4$ sites. As in previous studies, the DFT calculations support the idea that $Ni–N_3$ sites can enhance the activity of CO_2RR as well as inhibit HER. However, Ni–N–C-900 performs best in a flow cell test with a j_{CO} of 726 mA cm^{-2} and a CO FE of above 90%. This is because although $Ni–N_3$ sites are more active in CO_2-to-CO conversion and have better selectivity, high temperatures reduce the N and Ni atoms, thus significantly reducing the active site density. Notably, this work also discusses three possible configurations of NiN_3 sites: NiN_3, NiN_3C_1, and $NiN_{3\text{-vac}}$. Of the three NiN_3 sites modeled and the NiN_4 site, the $NiN_{3\text{-vac}}$ site has the largest positive $U_{L(CO2RR)} - U_{L(HER)}$ value, indicating that the $NiN_{3\text{-vac}}$ site could have high CO_2RR selectivity.

3.2.2 Creating vacancies. Ni SACs generally have impressive selectivity in CO_2-to-CO conversion among the reported catalysts, but some studies, such as the one above, have indicated that creating a vacancy can still further

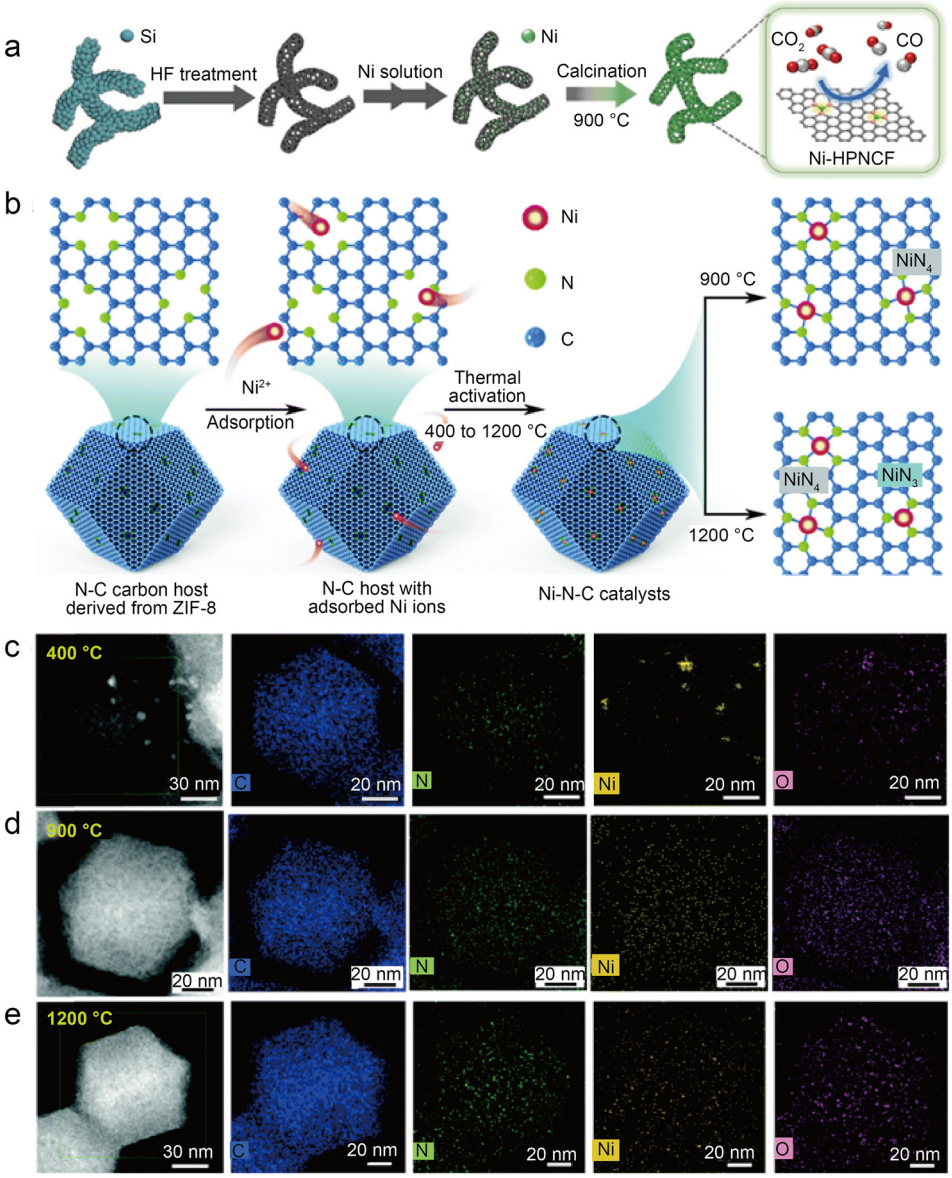

Fig. 8 (a) Schematic representation of the synthesis of Ni-HPNCF.[44] Reprinted with permission from Wiley-VCH, copyright 2023. (b) Synthesis scheme of the Ni–N–C catalysts using a nitrogen-doped carbon host to absorb Ni ions, followed by thermal activation at different temperatures to tune the Ni–N bond structures and establish the structure–property correlations; (c–e) HAADF-STEM and the corresponding EDS elemental mapping showing the homogeneous distribution of C, N, and Ni atoms on the surface for Ni–N–C activated at 900 °C and 1200 °C as compared to noticeable metallic clusters on Ni–N–C with 400 °C thermal activations. Temperature labels indicate activation temperature; samples were characterized at room temperature.[45] Reprinted with permission from Royal Society of Chemistry, copyright 2022.

increase the selectivity. Most reported strategies first introduce heteroatom coordination to form complex precursors and subsequently remove heteroatoms at high temperatures to create vacancies. This is a complex process with demanding reaction conditions. Jia *et al.*[46] proposed a facile method (Fig. 9a) for creating nitrogen vacancies (NV) on the Ni–N–C catalyst by continuous microwave-induced plasma strikes. Upon the induction of NV, the Ni site is converted to a steady Ni–N_2 coordination configuration with pyridinic N-dominance, which promotes the kinetic of CO_2-to-CO conversion. The plasma treatment duration is significant, as adequate treatment time can generate nitrogen vacancies in the Ni-SAC (SA-NiNG-NV) by inducing the reconstruction of coordinated N atoms. For comparison, a 5 s plasma-treated catalyst, SA-NiNG, was prepared. These two catalysts are free of Ni NPs, and Ni atoms are uniformly dispersed on the carbon framework, which is demonstrated by TEM, XRD, HAADF-STEM and EDS (Fig. 9b–e). In the Raman spectra, SA-NiNG-NV shows higher I_D/I_G (ratio of D band intensity to G band intensity), supporting the presence of more defects. Moreover, SA-NiNG-NV displays fewer Ni–N species and N contents in the XPS spectra compared with SA-NiNG, which is consistent with the Raman spectra. According to the FT-EXAFS fitting results, in SA-NiNG-NV, the

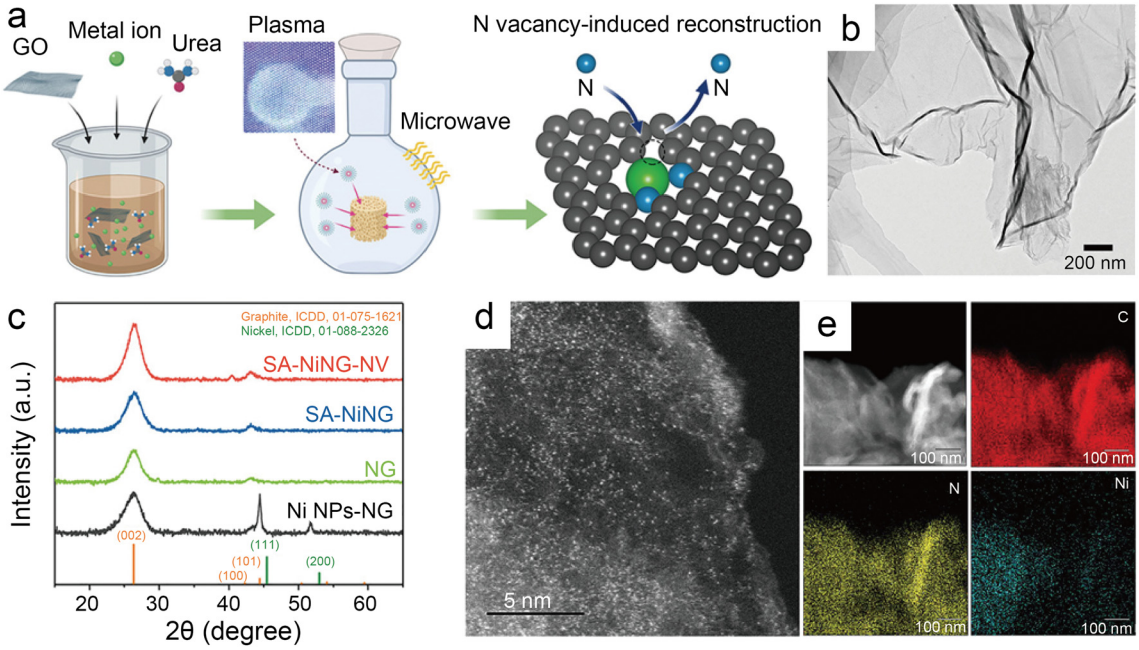

Fig. 9 (a) Schematic illustration of microwave induced plasma-assisted synthesis for SACs; (b) transmission electron microscopy (TEM) image of SA-NiNG-NV; (c) X-ray diffraction (XRD) patterns of both catalysts SA-NiNG and SA-NiNG-NV, and control samples N-doped graphene (NG) and metallic Ni nanoparticles decorated NG (Ni NPs-NG); (d) high-angle annular dark field scanning transmission electron microscopy (HAADF-STEM) image of SA-NiNG-NV; and (e) EDS mapping images of SA-NiNG-NV.[46] Reprinted with permission from Wiley-VCH, copyright 2021.

unsaturated Ni-pyridinic N_2V_2 structure is formed by each Ni atom being coordinated to an average of two N atoms. However, in SA-NiNG, the Ni-pyrrolic N_3–C defective coordination structure is formed by the involvement of three N atoms in the coordination formation. Combined with the DFT calculation, this leads to the conclusion that the unsaturated local coordination environment provides sufficient space for the adsorption of CO_2, while the defective graphene planes reduce the ability to constrain the Ni atoms, resulting in the active sites being more likely to shift outwards and bind to CO_2 molecules. Electrochemical performance test data suppose that the introduction of NVs significantly improves the performance of the catalyst towards CO_2RR. In the potential window ranging from −0.5 to −1.0 V, the maximum value of CO FE increases from 91.2% to 96.4%. The higher turnover frequency (TOF) reflects the enhanced intrinsic activity of SA-NiNG-NV.

3.2.3 Diversifying coordination atom species. In addition to N atoms, the introduction of secondary heteroatoms, such as S and P, into SACs can also change both the coordination number and electronic structure of central metal atoms. The electronic structure is strongly influenced by the first coordination domains. Besides, the electron localization around the active sites can be optimized by modifying the binding band of the second coordination domains. Hu *et al.*[15] optimized the interaction of the active sites and key intermediates by synergizing the long-range axial coordination regulation of S atoms within the first coordination domain and the near-range regulation of P atoms within the second coordination domain. Consequently, the CO FE of the Zn SAC is approximately 100%. Jia *et al.*[47] reported a method for obtaining a unique unsaturated NiN_2–S coordination structure *via* microwave-induced plasma. The electronic structure around Ni atoms changes significantly owing to the coordinated N and S atoms, as well as the vacancies and defective sites. Synthetic NiNG–S catalysts display high electrochemical activity and selectivity. In an H-cell, NiNG–S displays a maximum CO FE of 97% at −0.8 V and a largest j_{CO} of 40.3 mA cm^{-2} at −0.9 V. Ni K-edge XAS spectra demonstrate that S atoms could drop off easily and form vacancies (denoted as NiN_2-VS) at high potential, therefore confirming the potential-dependent stability of NiN_2–S sites. However, NiNG–S with NiN_2-VS structure still exhibits superior electrochemical properties than NiNG. DFT calculations reveal that both NiN_2–S and NiN_2-VS can reduce the energy barriers of CO_2–CO conversion, thus demonstrating outstanding performance.

Besides modulating the planar coordination environment of the Ni atom on the carbon network, the insertion of axial heteroatom coordination is also an effective strategy. According to the principles of organometallics, the Ni^{II} (*i.e.*, the d^8 species) has a strong tendency to form D_{4h} square planar geometries and is less capable of forming axial bonds.[63] For this reason, precise synthesis of M–N_4–O structure with axial M–O coordination is an extremely difficult task. In classic biological substances with Fe–N_4–Cl and Fe–N_5 structures, the heterogeneous and metal atoms form specific coordination sites on the parallelogram. Inspired by this, Wang *et al.*[48] modelled biological structures *via* an axial traction strategy (Fig. 10a). The XRD together with the TEM demonstrates that metal

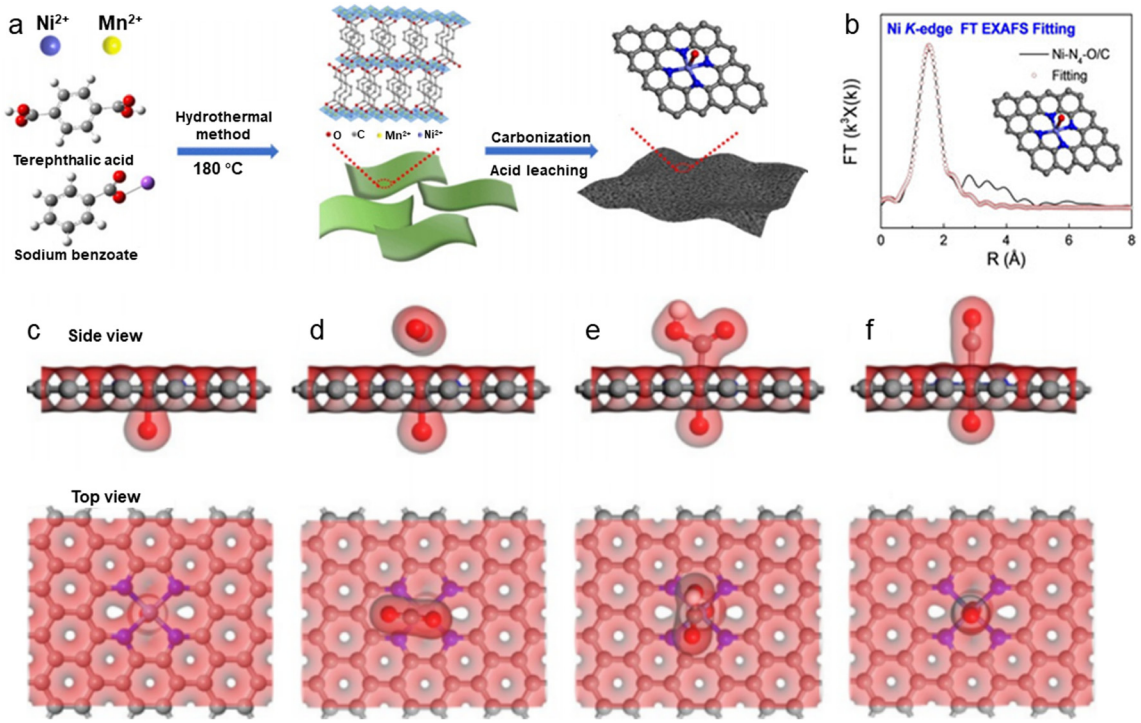

Fig. 10 (a) Illustration of the synthesis process; (b) EXAFS fitting curves in *R* space. Inset: Corresponding schematic model of Ni–N_4–O/C; (c)–(f) side view and top view of structural evolution of electrochemical CO_2RR for Ni–N_4–O/C (Ni cyan, N blue, O red, H white, C grey).[48] Reprinted with permission from Wiley-VCH, copyright 2020.

nanoparticles are effectively removed by acid-leaching treatment. The EDX element mapping images combined with XPS verify that coexisting N, O, and Ni atoms are uniformly dispersed on carbon substrates. According to the results of AC-STEM, EXAFS, EXANES and DFT calculations, it is concluded that four nitrogen atoms and one axial oxygen atom anchor the atomically dispersed Ni sites (inset of Fig. 10b). The Ni–N_4–O/C electrocatalyst exhibits superior ECR performance with a maximum of 99.2% CO FE at −0.9 V. The CO FE can remain above 90% in a potential window ranging from −0.5 to −1.1 V, which is a wider range than that of conventional catalysts (−0.5 to −0.9 V). In comparison with the Ni–N_4–PRO/C without an axial O atom, the extraordinary CO_2RR activity of Ni–N_4–O/C is further demonstrated to be due to the axial traction effect induced by the axial oxygen atom and the Ni–N_4 site. Furthermore, this work proposes that, unlike the typical Ni–N_4/C catalysts, the CO_2 molecules react on the backside of graphene rather than on the side containing O atoms (Fig. 10c–f). Huang *et al.*[49] reported a one-pot template-sacrificing pyrolysis strategy by decomposing the $Mg(OH)_2$ template to create highly porous structures and synthesize catalysts with the same Ni–N_4–O structure, as described above (Fig. 11a). At −0.76 V, the NiSA(0.3)-N-PGC shows a maximum CO FE of 97.2%. Overall experimental and theoretical calculations conclude that the outstanding properties are attributed to the induced charge asymmetry distribution and the higher electronegativity of the axially coordinated O atoms, which enhance the electronic delocalization at the central metal atom sites, resulting in lowering Gibbs free energy of the rate-limiting step, strengthening the bonding with *COOH, and weakening the bonding with *CO. In addition, porous structures formed by interlinked conductive mesh structures and interconnected thin plates with large specific surface areas greatly facilitate mass transport.

The introduction of heteroatoms into the coordination structure not only affects the electron distribution of the central Ni atoms, but in some cases, the heteroatoms also coordinate with the Ni atoms to form dual site active centers, synergistically regulating the interaction with the reaction intermediates. Ma *et al.*[64] investigated 27 types of catalysts with the structure of Ni–$B_XC_YN_Z$ ($X + Y + Z = 4$) *via* DFT calculations. B acts like a transition metal in many cases because its incompletely occupied valence electron d-orbital is so conducive to accepting and donating lone pairs of electrons. The results indicate that with the introduction of B, the Ni and B atoms are coordinated to form a dual active site, leading to various single or dual site adsorptions of reaction species. Consequently, the linear scaling relationship between *CO and *COOH adsorption is obviously diminished. Notably, in contrast to Ni–$B_XC_YN_Z$ ($X = 0$), the potential-determining step of Ni–$B_XC_YN_Z$ ($X \neq 0$) changes to *CO desorption rather than *COOH formation. Overall, this work displays the tremendous potential of B to improve the CO_2RR performance of Ni SACs. However, to the best of our knowledge, this structure has not yet been applied in experiments. It remains a great challenge.

As a transition metal, Ni has strong binding with H atoms, which enhances HER. Hu *et al.*[65] introduced HER-inert In atoms to modulate the electronic structure of Cu atoms,

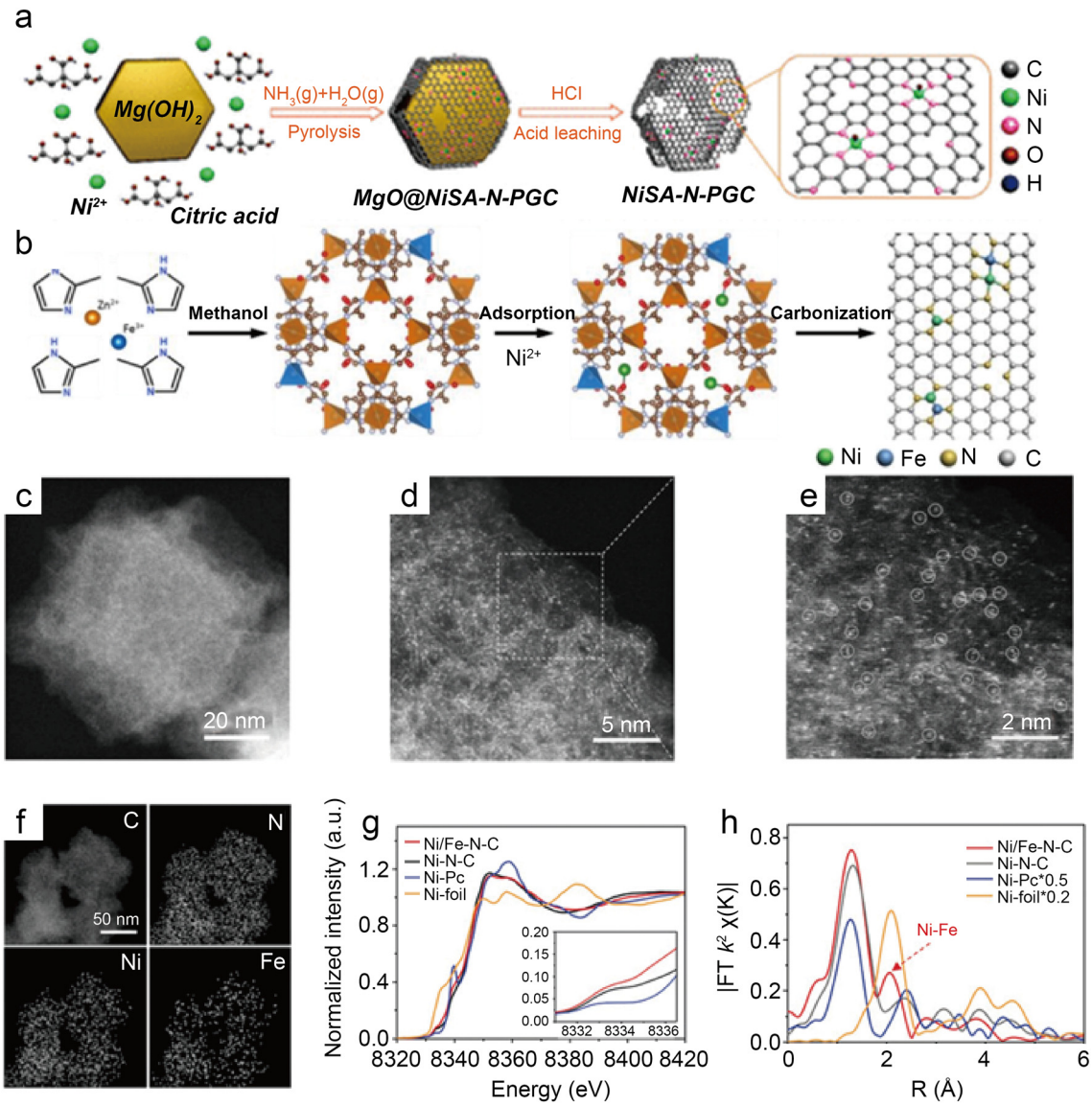

Fig. 11 (a) Illustration of the synthesis of nickel single nickel atoms dispersed on nitrogen-doped porous graphitic carbon (NiSA-N-PGC).[49] Reprinted with permission from American Chemical Society, copyright 2022; (b) scheme of the synthesis of Ni/Fe–N–C; (c) HAADF-STEM image; (d and e) enlarged HAADF-STEM images of Ni/Fe–N–C; (f) elemental mapping of Ni/Fe–N–C; (g) Ni K-edge XANES spectra of Ni/Fe–N–C, Ni–N–C, Fe–N–C, and Ni foil; and (h) Fourier transformation of the EXAFS spectra at *R* space.[50] Reprinted with permission from Wiley-VCH, copyright 2019.

which suppress HER while promoting CO_2RR. This strategy proves that modulating the binding energy of single-atom sites with key intermediates by leading in different metal atoms is a promising approach. For instance, Ren *et al.*[50] prepared the Ni/Fe–N–C by pyrolyzing the zeolitic imidazolate framework (Fig. 11b). Observations by HAADF-STEM and EDS analyses illustrate that single Ni and Fe atoms are homogeneously distributed without forming NPs (Fig. 11c–f). The analysis of XANES reveals distorted D_{4h} symmetry in Ni/Fe–N–C and presumes that the D_{4h} symmetry is distorted by another ligand (Fig. 11g). According to the Fourier transform (FT) k^2-weighted $\chi(k)$ function of the EXAFS spectra, Ni/Fe–N–C has a distinct metal–metal peak at 2.06 Å, which is not found in pure Fe–N–C and Ni–N–C, confirming the presence of Ni–Fe coordination (Fig. 11h). In a wide potential ranging from −0.5 to −0.9 V, the Ni/Fe–N–C catalyst displays excellent selectivity for CO FE with over 90% and reaches a peak of 98% at−0.7 V. After 30 hours of electrocatalysis, it also shows impressive stability by retaining 99% initial selectivity. The TOF at −1.0 V of Ni/Fe–N–C (7682 h^{-1}) is significantly larger than that of Fe–N–C (813 h^{-1}) and Ni–N–C (3690 h^{-1}), representing highly enhanced activity. The lower Tafel slope of Ni/Fe–N–C demonstrates the greatly enhanced kinetics of the rate-determining step. DFT calculations demonstrate that the Ni–Fe dual center can dramatically lower the reaction barrier, resulting in robust electrode durability. Moreover, when the monovalent Ni atom with the d^9 electronic configuration performs as the catalytic active site, the intrinsic CO_2RR activity of Ni SACs can be effectively enhanced.[66] Zhu *et al.*[51] designed a Ni–Cu coupled atom pair

with a Ni 3d electronic configuration (Ni/Cu–N–C), which shows a high TOF of 20 695 h^{-1} at −0.6 V with a maximum FE CO of 97.7%. The results of the XAS indicate that the Ni(I) species of Ni–Cu structures are the active sites for CO_2RR. The Cu element is more electro-negative; thus, the d-orbital energy level of the Ni site can be increased while combining with Cu.[67] Consequently, intermediates are more easily adsorbed because of anti-bonding states away from the Fermi energy level. The Ni–Cu structure greatly reduces the reaction potential and promotes CO_2RR kinetics simultaneously. Recently, many studies about coordinating Ni sites with metallic atoms have been reported, and the communitive effect between adjacent single atoms is considered essential for improved catalysis.

3.3 Surface modification

Regulation of coordination structures is the most straightforward way to alter the electronic distribution of central Ni atoms. In addition, non-coordinated regulation is a promising pathway for optimizing the electrocatalytic performance of Ni SACs. Specifically, it includes the structural modulation of the catalyst and reaction interface engineering.

3.3.1 Structure modulation of catalysts. N-doped carbon is regarded as the most common support for SACs. Most reported studies mainly focus on the single role of unsaturated coordinated M–N structures in improving the catalytic behavior of electrocatalysts by breaking the symmetrical electronic structure of nickel. However, Zheng *et al.*[52] found that the abundant electronegative N dopants around Ni–N_3 sites can modify the first neighboring C atoms of these sites, thus speeding up the CO_2RR kinetics process. In this work, Zheng *et al.* developed an electrocatalyst (denoted as Ni-N_3-NCNFs) using polyacrylonitrile (PAN) and dicyandiamide (DCDA) as the abundant N source. Ni-N_3-NCNFs display a high reaction kinetic in CO_2RR with a 71 mV dec^{-1} Tafel slope (Fig. 12a). XPS measurements prove the existence of Ni-pyridinic N and many extra N dopants (Fig. 12b). In comparison with Ni-NCNTs, which have low N resources, sufficient N doping also plays a crucial role in preventing the aggregation of Ni atoms. The results of WT-EXAFS, FT-EXAFS, and XANES clarify that the coordination of Ni atoms of Ni-N_3-NCNFs is a Ni–N_3 structure with D_{3h} symmetry, as shown in the inset of Fig. 12c, rather than a typical Ni–N_4 structure (D_{4h} symmetry). By constructing the Ni–N_3@C, Ni–N_3/GN@C, and Ni–N_3/PN@C model and calculating the free energy distributions of CO_2RR and HER at the Ni–N_3 sites, it can be concluded that the extra doping N alters the electronic structures of C atoms, which affect the adsorption of intermediates and the desorption of products, therefore improving the kinetics of CO_2RR and water dissociation. This work reveals that a non-coordinated heteroatom is promising for regulating the electronic structures of active sites.

Wang *et al.*[53] found that the addition of cyano to carbon-based substrates significantly facilitates the activation of CO_2. As shown in Fig. 12d, the cyano-modified catalyst, designated as Ni@C_3N_4–CN, is prepared by salt-assisted and calcination methods. Solid-state ^{13}C MAS NMR (Fig. 12e) and Fourier transform infrared (FT-IR) (Fig. 12f) demonstrate the existence of the –CN group in the carbon support. FT-EXAFS indicates the presence of Ni–N_4 configuration in Ni@C_3N_4–CN, also further confirming that the optimization of performance is not derived from changes in active site structures (Fig. 12g). The results of DFT calculations suppose that the formation of CN groups weakens d–π conjugation between the metal atoms and the supports, thus reducing the charge transfer from the metal atoms to the supports and increasing the electron density around the central metal atoms. In the H-cell electrochemical test at −1.178 V, Ni@C_3N_4–CN enables remarkable TOF of ∼22 000 h^{-1} and j_{CO} of 46.8 mA cm^{-2}. The CO FE is maintained above 90% even with a CO_2 concentration of only 30%. When operating at −0.93 V in the flow cell with pure CO_2, Ni@C_3N_4–CN displays −300 mA cm^{-2} current density with a CO FE of over 90%.

3.3.2 Reaction interface engineering. Pyrolysis is the most popular method of preparing SACs.[68–70] Precursors typically include metal salts, metal–organic frameworks (MOFs), substrates, such as graphene and carbon nanotubes, and metal NPs on the substrate. Under high-temperature pyrolysis, the metal nanoparticles disperse on the substrates at the atomic level. Consequently, some NPs are inevitably present on SACs.[71] Liang *et al.*[54] investigated the effect of Ni NPs on CO_2RR. They prepared a series of Ni-NG SACs with different amounts of nickel salts as precursors, denoted as $Ni_{1.11}$-NG, $Ni_{0.37}$-NG, and $Ni_{0.037}$-NG. SEM images show a 3D morphology composed of CNTs and porous NSs (Fig. 13a–c). Some exposed Ni NPs can be recognized in $Ni_{1.11}$-NG and $Ni_{0.37}$-NG, which is further supported by HAADF-STEM and EDS (Fig. 13d–f). HRTEM and XPS reveal the co-existence of single Ni atoms, exposed Ni NPs and encapsulated Ni NPs in Ni-NG. According to the XPS and ICP, the content of atomically dispersed Ni follows the order $Ni_{0.037}$-NG > $Ni_{0.37}$-NG > $Ni_{1.11}$-NG, which is in contrast to the order of the content of NPs. The three Ni-NG electrocatalysts show electrocatalytic activity towards CO_2RR. In the potential ranging from −0.5 V to −1.3 V, CO FE follows the order $Ni_{0.037}$-NG > $Ni_{0.37}$-NG > $Ni_{1.11}$-NG (Fig. 13g), suggesting that single Ni atoms are more conducive to CO_2RR than NPs. Furthermore, using strong acid to leach out most Ni NPs, the samples obtained are denoted as Ni-NG-H catalysts. The CO FE of Ni-NG-H catalysts even slightly increases (Fig. 13h and i), further indicating that Ni NPs are inactive to CO_2RR. However, Wang *et al.*[55] discovered that ultra-thin N-doped carbon shells encapsulating Ni NP catalysts (Ni@N–C) have superior electrochemical properties. When operating at −1.1 V in the flow cell, Ni@N–C displays excellent CO FE of 97% with 244 mA cm^{-2} industry-level current density. The impressive performance is due to the synergistic effects between the encapsulated Ni NPs and the N-doped carbon shell, which enhance CO_2 adsorption, promote electron transfer and expand the exposure of active sites. This work demonstrates the potential to improve catalytic performance by tuning the electronic structure of NPs.

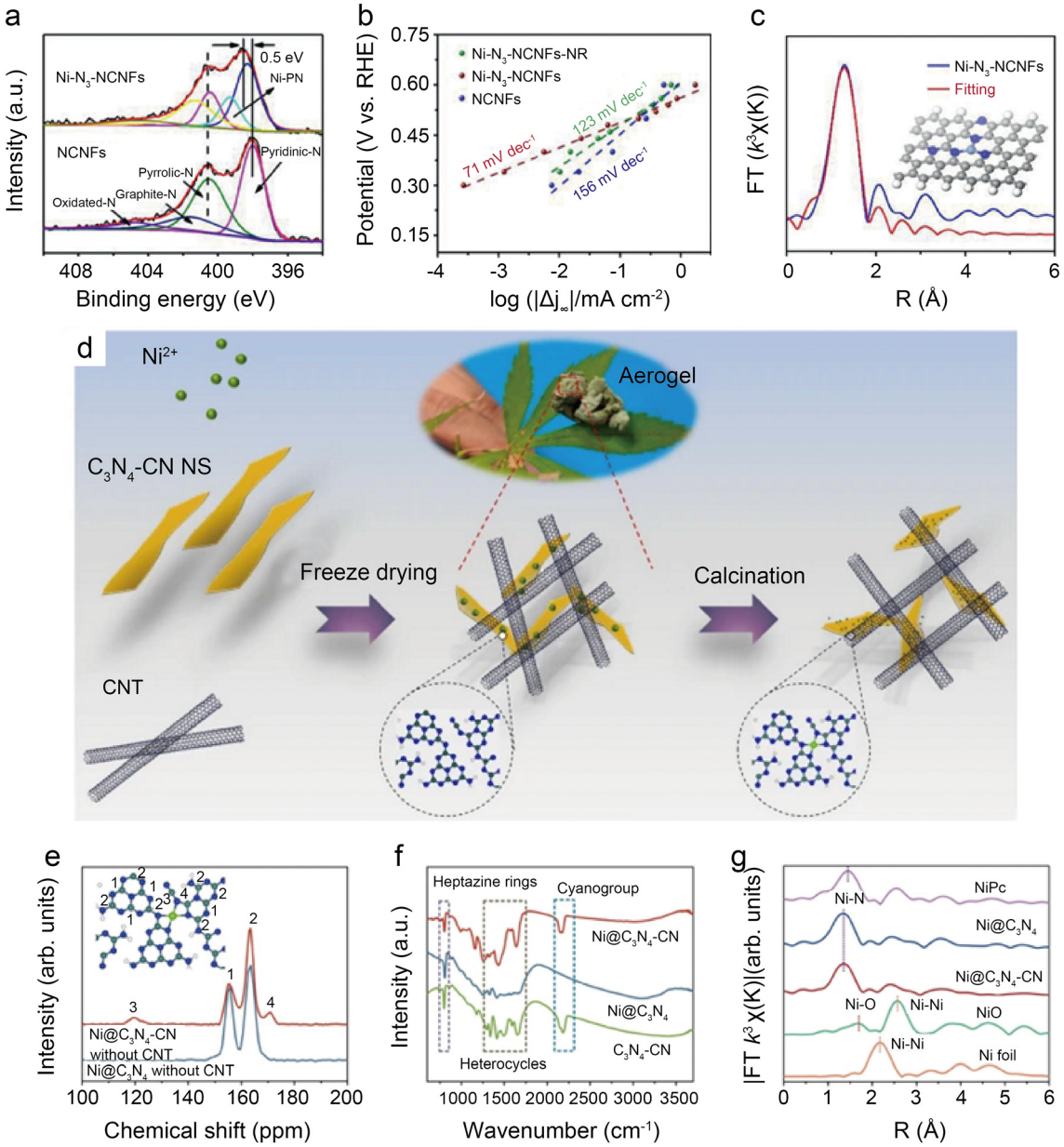

Fig. 12 (a) Tafel slopes of Ni-N_3-NCNFs-NR, Ni-N_3-NCNFs, and NCNFs; (b) high-resolution N 1s spectra of Ni-N_3-NCNFs and NCNFs; (c) fitting results for FT-EXAFS of Ni-N_3-NCNFs, inset: optimized model for Ni-N_3-NCNFs.[52] Reprinted with permission from Wiley-VCH, copyright 2021; (d) schematic illustration of the preparation; (e) solid-state ^{13}C MAS NMR spectra of Ni@C_3N_4–CN, Ni@C_3N_4 without CNT; (f) FT-IR spectra of Ni@C_3N_4–CN, Ni@C_3N_4 and C_3N_4–CN catalyst; and (g) k^3 weighted Fourier transform spectra from EXAFS of Ni@C_3N_4–CN and Ni@C_3N_4.[53] Reprinted with permission from Nature, copyright 2022.

If single atoms and nanoparticles can synergistically promote CO_2RR, then the complex post-treatment steps used to remove the nanoparticles are eliminated.

Using a brief Ni-metal organic framework-assisted method (Fig. 14a), Wen *et al.*[56] prepared a series of Ni(NC)-based catalysts formed by different contents of Ni NPs and single Ni atoms. The EDS images demonstrate that the Ni atoms are uniformly dispersed in Ni(NC)-1, and the existence of Ni NPs is also confirmed by the presence of bright spots in some areas with the combination of HRTEM (Fig. 14b and c). Several characterization results indicate that Ni(NC)-1 contains more N elements and therefore modulates the electronic structure of surface Ni species. In contrast, more unmodified Ni–Ni species are present on the carbon layers of Ni(NC)-2 and Ni(NC)-3. Consequently, Ni(NC)-1 exhibits considerably more extraordinary electrochemical performance (Fig. 14d and e). In the flow cell, Ni(NC)-1 shows 99% maximum CO selectivity with a large j of −160 mA cm^{-2} at −1.82 V. This work demonstrates the possibility of activating electrocatalytically inactive sites into active sites by modulating the electronic environment of Ni species. However, the detailed functions of NPs and single-atom sites in CO_2RR remain unclear. Bai *et al.*[57] claimed that Ni NPs

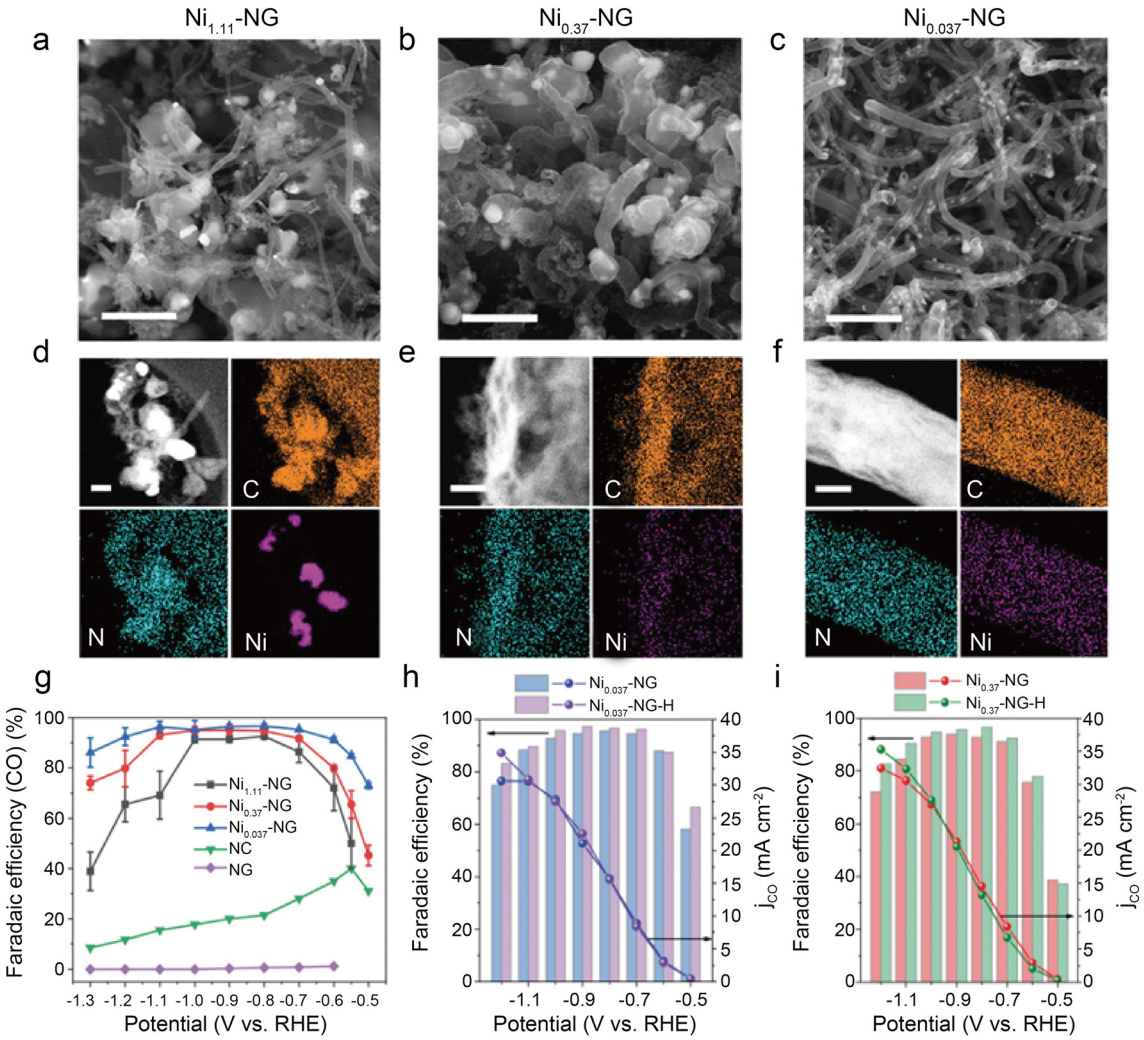

Fig. 13 (a–c) SEM images showing abundant carbon-encapsulated Ni NPs, scale bar: 1 μm; (d–f) HAADF-STEM images and the corresponding EDS elemental mapping of C, N, Ni, scale bar: 200, 50, and 50 nm for (d–f), respectively; (g) the CO FEs of catalysts loaded on glassy carbon electrode at independent potentials ranging from −0.5 to −1.3 V (*vs.* RHE); (h and i) the CO FEs and CO partial current densities of Ni-NG and Ni-NG-H catalysts loaded on carbon paper (CP) at independent potentials from ranging −0.5 to −1.2 V (*vs.* RHE).[54] Reprinted with permission from Wiley-VCH, copyright 2021.

promote the decomposition of H_2O to form *H, making it easier for adsorbed CO_2 molecules to generate *COOH through PCET, while Ni single-atom sites can stimulate CO_2 activation and CO desorption.

Some of the above works have proved that the coordination of the O atoms and the central Ni atoms can effectively break the symmetry of the electron density of the Ni–N_4 sites to improve catalytic performance. However, the precise construction of the M–N_x–O structure remains a great challenge. Recently, it has been demonstrated that O atoms can modulate the performance of catalysts in the form of highly dispersed metal oxide particles without participating in coordination.[72] Li *et al.*[58] designed a simple carbonization coupled oxidation method for synthesizing NiO/Ni–N–C SACs modified with NiO clusters (Fig. 15a). HAADF-STEM images indicate the presence of NiO clusters, Ni NPs and Ni single atoms (Fig. 15b–d). The EDS images further reflect the uniform scatter of the N, Ni, and C elements on the carbon substrate (Fig. 15e). Analysis of XRD and XPS images leads to the conclusion that the Ni species are mainly present in the form of coordinated Ni–O and highly dispersed Ni–N sites in NiO/Ni–N–C-800, which is in agreement with the results of XAS, EXAFS, XANES and other characterization techniques. In a wide potential ranging from −0.9 to −1.3 V, the CO FE of NiO/Ni–N–C-800 remains over 90% (Fig. 15f). At −1.1 V, CO FE reaches a peak of 93%. The DFT calculation proposes greater properties of NiO/Ni–N–C-800 (Fig. 15g and h) because the NiO clusters reduce the energy barrier of CO_2–CO conversion by enhancing the electronic delocalization of active sites. Besides, the hierarchical porous morphology of NiO/Ni–N–C-800 facilitates mass transfer and exposes more accessible active sites. This work presents advanced insights into adjusting the electronic structure of active sites by oxygen modulation.

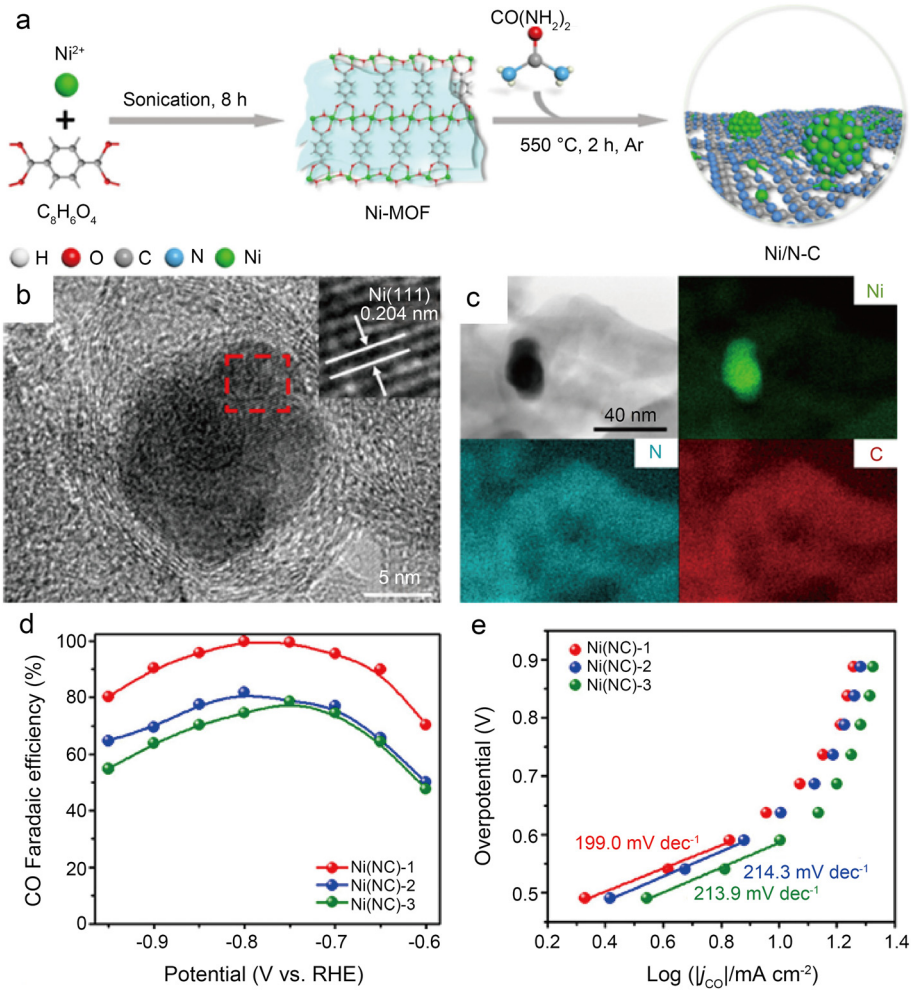

Fig. 14 (a) Schematic illustration of the formation of Ni(NC) samples; (b) HRTEM images of Ni(NC)-1. The inset of (b) is the enlarged HRTEM image showing the (111) lattice fringe of Ni; (c) bright-field TEM image of Ni(NC)-1 and the corresponding element mapping images of Ni, N, and C; (d) faradic efficiencies of CO for the samples at various applied potentials; and (e) Tafel plots of j_{CO} for the samples at various applied potentials.[56] Reprinted with permission from American Chemical Society, copyright 2019.

4 Summary and perspectives

4.1 Summary

The catalytic reduction of CO_2 into value-added fuels and chemicals *via* renewable electricity is accepted as an efficient solution to alleviating the energy crisis and greenhouse effect. SACs have received substantial research attention owing to their high atom utilization, abundant active sites and excellent catalytic performance. Besides, SACs have the advantages of both homogeneous and multiphase catalysis.[73] Regarding the central metals of SACs, transition metals are the best choice owing to their special electronic structures, which can provide vacant d-orbitals to combine the key intermediates and reduce the activation energy barrier of CO_2RR, thus increasing the intrinsic activity. CO_2RR has a wide range of products, of which CO is a key feedstock for Fischer–Tropsch synthesis and is of high industrial value. In electrochemical tests, Ni SACs show more outstanding activity and selectivity than other transition metal SACs and therefore have been a hot topic of research. Based on DFT calculations and crystal field theory, the d-orbital of the central transition metal splits in a square planar field in the conventional M–N_4 structure of SACs, and Ni is more likely to form vacant outermost d-orbitals compared with other transition metals (*e.g.* Fe, Co, and Cu). Such vacant orbitals facilitate the transfer of electrons from the C atom of the CO_2 molecules to the Ni atom and promote the activation of liner CO_2. In addition, *in situ* spectroscopic and theoretical thermodynamic studies indicate that Ni SACs overcome the free energy potential barrier of the CO_2RR rate-determining step and benefit the generation of *COOH intermediates. Consequently, Ni SACs always have a higher selectivity for generating CO than other transition metal single-atom catalysts.

This review begins by describing the pathway of CO generation *via* CO_2RR and the characterization methods for determining the active site structures of Ni SACs. Following that, depending on different approaches to enhance

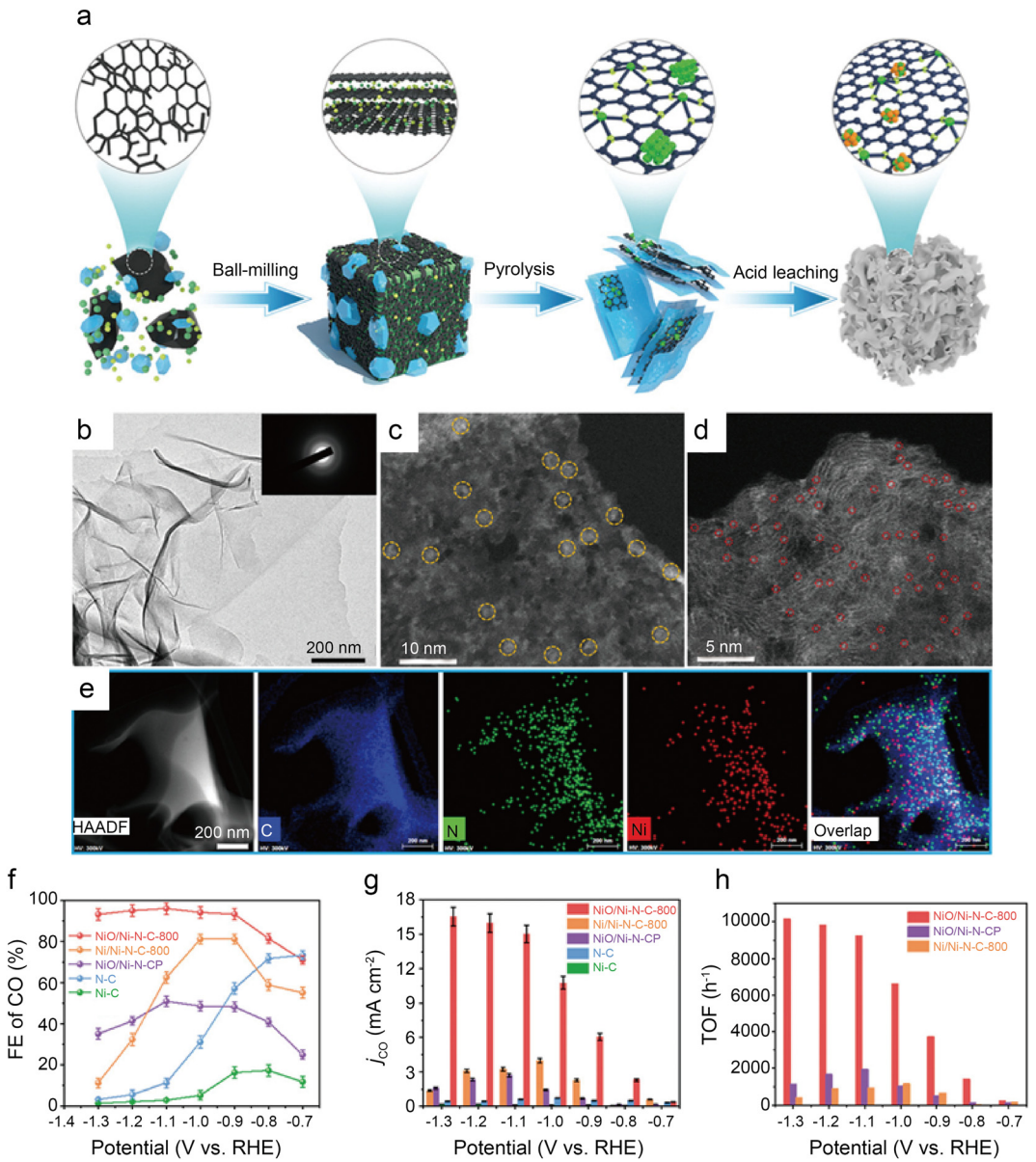

Fig. 15 (a) Schematic diagram of the synthesis process for NiO/Ni–N–C; (b) TEM image (inset: SAED pattern) of NiO/Ni–N–C-800; (c and d) HAADF-STEM images of NiO/Ni–N–C-800. The yellow circles are identified as NiO clusters, and the small red circles are identified as single Ni atoms; (e) EDS mapping images of NiO/Ni–N–C-800; (f) FECO for various samples at different potentials; (g) j_{CO} for various samples at different potentials; and (h) TOF of NiO/Ni–N–C-800, NiO/Ni–N–CP, and Ni/Ni–N–C-800 at different potentials.[58] Reprinted with permission from Wiley-VCH, copyright 2022.

electrocatalytic performance, the Ni SACs reported in recent years are divided into three groups:

(1) Different structures of supports. Carbon materials are popular catalyst substrates owing to their abundant sources, regulated structure, excellent chemical stability, and superior electrical conductivity. Besides their function as electrical conductors, carbon substrates also have an essential effect on the rate of mass transfer. Carbon black, graphene, and carbon nanotubes are examples of typical carbon substrates. To accelerate mass transfer and improve active site density, many substrates with a high specific surface area and many mesoporous channels are being explored for the synthesis of Ni SACs.

(2) Coordination structure regulation. Nitrogen-doped carbon facilitates the anchoring of central metal atoms and stabilizes coordination structures. The most common structure is Ni–N–C, with Ni–N_4 as the conventional active center coordination structure. However, the symmetrical electronic structure is detrimental to the PCET process and diminishes the kinetics of CO_2RR. Adjusting the coordination number, constructing vacancy defects, and varying the species of coordination atoms are prevalent strategies for breaking symmetric electronic structures. Among them, varying the species of coordination atoms includes the addition of dopants other than nitrogen on the carbon

substrates (S, P, *etc.*), the introduction of axial heteroatom coordination (O, Cl, *etc.*), and the insertion of metal atoms to form dual active centers with nickel (Fe, Cu, *etc.*).

(3) Surface modification. Changing the coordination structure is the most straightforward way to break the symmetry of the electron distribution, but altering the surface structure and composition is also an effective strategy. Nitrogen has strong electronegativity, and when doped in excess, it can affect the electron distribution of the C atoms adjacent to the active site, accelerating the kinetics of CO_2RR. The introduction of functional groups (*e.g.* –CN) on the substrate can boost the electron density of the active sites, thereby accelerating CO_2 activation. The preparation of SACs inevitably produces NPs, which are inactive for CO_2RR, but the addition of ultrathin N-doped carbon shells encapsulating Ni NPs and NiO clusters on the catalyst surface in appropriate amounts can enhance electrochemical performance.

4.2 Perspectives

Thus far, Ni–N–C has made outstanding progress in the direction of electrocatalytic reduction of CO_2 to CO, but there are still many problems to overcome. An excellent Ni SAC should also have excellent atom utilization, activity, selectivity and stability. Subsequently, some perspectives on the existing challenges are then discussed.

(1) Improving the singularity of coordination structures. The coordination structure is the most vital part of Ni SACs, yet regulating the microenvironment of the active center to synthesize active sites with a single coordination environment remains a great challenge. Currently, most reports attribute the average properties of the sample to overall catalytic performance, lacking rigor in demonstrating efficient active sites. Methods, such as flame spray pyrolysis, which provides a relatively homogeneous synthesis environment, hold the promise of achieving the singularity of coordination structures.

(2) Innovating coordination structure types. Recently, most studies have focused on modulating the coordination structure of SACs, which still fail to produce a significant increase in catalytic efficiency. The formation of super-coordinated structures using physical–chemical methods disrupting the original electronic structure equilibrium, replacing the species of coordination atoms and increasing or decreasing the number of coordination atoms of the active central atom in the catalytic material can change the intrinsic energy band structure, electrical conductivity and catalytic activity. It provides new opportunities to further improve the performance of catalysts. Both Fe–N_5 and Co–N_5 have been proven to greatly enhance catalytic activity,[74–76] but investigations on Ni–N_5 are still relatively few. The Ni–N_4–O structure with axial O coordination shows remarkable catalytic properties. Xiao *et al.*[77] have demonstrated that the Ni–N_4–O_2 structure has great promise for the electrosynthesis of H_2O_2, and it has great research value in applying this structure to CO_2RR. Ultra-high coordination has the potential to achieve a quantum leap in properties, and ultra-low coordination structures, such as Ni–N_2, are also well worth investigating.

(3) Designing multi-sites catalysts. DACs can not only reduce the activation barriers of CO_2RR but also break the linear scaling relation to further improve selectivity. Ni is often combined with other metal atoms to form dual-site catalysts, and owing to its special electronic structure, the catalysts always show good synergetic effects to promote catalytic efficiency. Therefore, expanding the number of active sites to create multi-site catalysts holds considerable promise. Moreover, if each site plays a distinct role, such as in one dual-site catalyst in which the Ni site is responsible for the adsorption of *COOH intermediates and the Cu site is used to promote C–C coupling, there is a possibility of generating multi-carbon products with high selectivity.

(4) Improving the loading of Ni. The loading of Ni is positively correlated with the intrinsic activity of the catalyst. However, according to the present reports, the loading of SACs is usually less than 5%. This is because it is difficult to improve the single-atom stability and inhibit the agglomeration of metal atoms while increasing the loading with the current synthesis methods. After a long reaction, Ni atoms tend to agglomerate to form nanoparticles that facilitate HER. Therefore, stabilizing the central metal atoms also contributes to the stability of the catalyst performance. Creating defects on the N-doped carbon substrates before inserting Ni atoms can help stabilize the structure of active sites, while microwave plasma induction and femtosecond lasers are all worthwhile synthetic approaches. To achieve industrial applications, it is not only desirable to increase the loading for achieving current densities for industrial applications (>200 mA cm^{-2}) but also to explore synthetic methods that can produce catalysts on a large scale.

(5) Developing more types of substrates. The framework of substrates considerably influences catalytic properties. However, it is still a challenge to expand the types of substrates, with N-doped carbon being the most common. Synthesizing single-atom alloys by loading metal atoms on metal substrates has the potential to display substantial synergistic effects, disrupt the linear scaling relation, and promote multiphase catalysis. Aerogels, for example, are three-dimensional porous structures with a huge surface area that improves the exposure of active sites, isolates metal atoms in space and inhibits agglomeration.

(6) Exploring more operando characterization techniques. CO_2RR involves complex PCET processes, and the development of *operando* characterization techniques is key to identifying the real active sites and tracking specific reaction pathways. Besides, *operando* characterization technologies can reveal the stability of the catalyst under reaction conditions, distinguish the species of key intermediates and clarify the influence of reaction conditions, which can be of great significance in designing catalysts with high activity for generating target products. To date, the main experimental approach to explore the CO_2RR mechanism is through the analysis of *ex situ*

characterization (TEM, XAS, XPS, *etc.*) of the catalyst before and after CO_2RR. However, surface reconstruction, morphological transformation and active site evolution usually occur during the reaction process, so these *ex situ* methods cannot capture important information about the real CO_2RR process. Although progress has been made in *in situ* IR, *in situ* Raman and *in situ* electron microscopy, the application is still limited. The small size of SACs makes it crucial to develop *in situ* techniques to directly observe the evolution of active sites at atomic resolution. Exploring more techniques, such as *in situ* SEM, which can visualize individual molecules and atoms adsorbed on the catalyst surface and monitor the configuration of intermediates in real-time, can help to clarify the catalytic mechanisms. Imaging the morphology and activity of the active center in conjunction with reaction devices is vital to reveal reaction mechanisms and design catalytic systems.

(7) Optimizing electrolytic cells. For electrochemical testing, H-cells and flow cells are the most popular choices. The H-cell is a simple device. However, the tank pressure is too high, and the test current density is limited. The flow cell is more compact when combined with a gas diffusion electrode, which significantly improves the mass transfer efficiency, but the energy efficiency and reaction life are still far from the industrial requirements. The membrane electrode assembly cell (MEA cell) has great industrial applications, as the cathode is separated from the anode only by an ion exchange membrane, which greatly reduces the internal resistance and increases the reaction efficiency, and has great prospects for industrial applications. However, there are still many issues that are worth discussing in terms of testing methods, such as feeding methods and electrode structures. Recently, the solid oxide electrolytic cell (SOEC) has gained popularity because of its advantages of high energy efficiency and high product selectivity. Importantly, under typical SOEC operating conditions, CO is the only product of CO_2RR. In addition, SOEC operates at high temperatures, which inhibits the formation of NPs from Ni SACs during the reaction. Furthermore, the use of SOECs to produce high-purity CO for CO reduction, such as cascade systems, is projected to produce multi-carbon products for upgrading the products.

(8) Investigating the microscopic mechanisms of electrolytes. The pH and ionic type of the electrolyte crucially affect the rate of mass transfer and the stability of the reaction intermediates. Because alkaline electrolytes can inhibit HER, cathodic electrolytes, such as $KHCO_3$, K_2CO_3, and KOH, are frequently used. However, alkaline electrolytes are prone to form carbonate, which harms single-pass CO_2 utilization. Acidic electrolytes have the potential to increase single-pass CO_2 utilization but are prone to HER. The addition of alkali metal ions to a strongly acidic electrolyte has been confirmed to inhibit HER. Recently, ionic liquid (IL) electrolytes have attracted attention owing to their high CO_2 solubility.[78] The IL electrolytes can modulate the three-phase interface and significantly increase the current density while increasing the single-pass CO_2 utilization. Furthermore, bulk ionic liquid electrolytes have high viscosity, slow diffusion rate and low ionic conductivity. When added to Ni SACs with porous structures, they can develop the secondary co-catalyst phase and improve catalytic performance. Ni SACs still have many growth opportunities and are expected to play a more active role in CO_2RR in the future.

Author contributions

ZiYan Yang: conceptualization, writing-original draft. Rongzhen Chen: writing-review and editing. Ling Zhang: supervision. Yuhang Li: supervision, writing-review and editing. Chunzhong Li: supervision.

Conflicts of interest

There are no conflicts to declare.

Acknowledgements

This work was supported by the National Natural Science Foundation of China (22322805, 22178104, U22B20143), Shanghai Municipal Science and Technology Major Project, the Shanghai Scientific and Technological Innovation Project (22dz1205900), "the Fundamental Research Funds for the Central Universities", and Shanghai Rising-Star Program (23QA1402200).

References

1 J. Zhang, C. Guo, S. Fang, X. Zhao, L. Li, H. Jiang, Z. Liu, Z. Fan, W. Xu, J. Xiao and M. Zhong, Accelerating electrochemical CO_2 reduction to multi-carbon products via asymmetric intermediate binding at confined nanointerfaces, *Nat. Commun.*, 2023, **14**, 1298.
2 J. Gao, A. Bahmanpour, O. Kröcher, S. M. Zakeeruddin, D. Ren and M. Grätzel, Electrochemical synthesis of propylene from carbon dioxide on copper nanocrystals, *Nat. Chem.*, 2023, **15**, 705–713.
3 S. Wang, L. Wang, D. Wang and Y. Li, Recent advances of single-atom catalysts in CO_2 conversion, *Energy Environ. Sci.*, 2023, **16**, 2759–2803.
4 S. Das, J. Pérez-Ramírez, J. Gong, N. Dewangan, K. Hidajat, B. C. Gates and S. Kawi, Core-shell structured catalysts for thermocatalytic, photocatalytic, and electrocatalytic conversion of CO_2, *Chem. Soc. Rev.*, 2020, **49**, 2937–3004.
5 S. Dongare, O. K. Coskun, E. Cagli, K. Y. C. Lee, G. Rao, R. D. Britt, L. A. Berben and B. Gurkan, A bifunctional ionic liquid for capture and electrochemical conversion of CO_2 to CO over silver, *ACS Catal.*, 2023, **13**, 7812–7821.
6 P.-C. Chen, C. Chen, Y. Yang, A. L. Maulana, J. Jin, J. Feijoo and P. Yang, Chemical and structural evolution of AgCu catalysts in electrochemical CO_2 reduction, *J. Am. Chem. Soc.*, 2023, **145**, 10116–10125.
7 M.-G. Kim, J. Park, Y. Choi, H. C. Song, S.-H. Kim, K.-M. Bang, H. C. Ham, N.-K. Kim, D. H. Won, B. K. Min, S. J. Yoo and W. Kim, Cuir nanoparticles for electrochemical

reduction of CO_2 to t-BuOH, *Adv. Energy Mater.*, 2023, **13**, 2300749.

8 Y. Jia, H.-S. Hsu, W.-C. Huang, D.-W. Lee, S.-W. Lee, T.-Y. Chen, L. Zhou, J.-H. Wang, K.-W. Wang and S. Dai, Probing the roles of indium oxides on copper catalysts for enhanced selectivity during CO_2-to-CO electrochemical reduction, *Nano Lett.*, 2023, **23**, 2262–2268.

9 K. Zhang, J. Wang, W. Zhang, H. Yin, J. Han, X. Yang, W. Fan, Y. Zhang and P. Zhang, Regulated surface electronic states of CuNi nanoparticles through metal-support interaction for enhanced electrocatalytic CO_2 reduction to ethanol, *Small*, 2023, **19**, 2300281.

10 Y. Xu, Y. Guo, Y. Sheng, H. Yu, K. Deng, Z. Wang, X. Li, H. Wang and L. Wang, Selective CO_2 electroreduction to formate on polypyrrole-modified oxygen vacancy-rich Bi_2O_3 nanosheet precatalysts by local microenvironment modulation, *Small*, 2023, **19**, 2300001.

11 M. G. Lee, X.-Y. Li, A. Ozden, J. Wicks, P. Ou, Y. Li, R. Dorakhan, J. Lee, H. K. Park, J. W. Yang, B. Chen, J. Abed, R. dos Reis, G. Lee, J. E. Huang, T. Peng, Y.-H. Chin, D. Sinton and E. H. Sargent, Selective synthesis of butane from carbon monoxide using cascade electrolysis and thermocatalysis at ambient conditions, *Nat. Catal.*, 2023, **6**, 310–318.

12 K. Qi, Y. Zhang, N. Onofrio, E. Petit, X. Cui, J. Ma, J. Fan, H. Wu, W. Wang, J. Li, J. Liu, Y. Zhang, Y. Wang, G. Jia, J. Wu, L. Lajaunie, C. Salameh and D. Voiry, Unlocking direct CO_2 electrolysis to C_3 products via electrolyte supersaturation, *Nat. Catal.*, 2023, **6**, 319–331.

13 M. B. Ross, P. De Luna, Y. Li, C.-T. Dinh, D. Kim, P. Yang and E. H. Sargent, Designing materials for electrochemical carbon dioxide recycling, *Nat. Catal.*, 2019, **2**, 648–658.

14 Y. Y. Birdja, E. Pérez-Gallent, M. C. Figueiredo, A. J. Göttle, F. Calle-Vallejo and M. T. M. Koper, Advances and challenges in understanding the electrocatalytic conversion of carbon dioxide to fuels, *Nat. Energy*, 2019, **4**, 732–745.

15 C. Hu, Y. Zhang, A. Hu, Y. Wang, X. Wei, K. Shen, L. Chen and Y. Li, Near- and long-range electronic modulation of single metal sites to boost CO_2 electrocatalytic reduction, *Adv. Mater.*, 2023, **35**, 2209298.

16 S. C. Sarma, J. Barrio, A. Bagger, A. Pedersen, M. Gong, H. Luo, M. Wang, S. Favero, C.-X. Zhao, Q. Zhang, A. Kucernak, M.-M. Titirici and I. E. L. Stephens, Reaching the fundamental limitation in CO_2 reduction to CO with single atom catalysts, *Adv. Funct. Mater.*, 2023, **33**, 2302468.

17 S. Chen, J. Chen, Y. Li, S. Tan, X. Liao, T. Zhao, K. Zhang, E. Hu, F. Cheng and H. Wang, Fe-N_4O-C nanoplates covalently bonding on graphene for efficient CO_2 electroreduction and Zn-CO_2 batteries, *Adv. Funct. Mater.*, 2023, **33**, 2300801.

18 J. Wang, Y.-C. Huang, Y. Wang, H. Deng, Y. Shi, D. Wei, M. Li, C.-L. Dong, H. Jin, S. S. Mao and S. Shen, Atomically dispersed metal–nitrogen–carbon catalysts with d-orbital electronic configuration-dependent selectivity for electrochemical CO_2-to-CO reduction, *ACS Catal.*, 2023, **13**, 2374–2385.

19 Y. Zhou, A. J. Martín, F. Dattila, S. Xi, N. López, J. Pérez-Ramírez and B. S. Yeo, Long-chain hydrocarbons by CO_2 electroreduction using polarized nickel catalysts, *Nat. Catal.*, 2022, **5**, 545–554.

20 S. Nitopi, E. Bertheussen, S. B. Scott, X. Liu, A. K. Engstfeld, S. Horch, B. Seger, I. E. L. Stephens, K. Chan, C. Hahn, J. K. Nørskov, T. F. Jaramillo and I. Chorkendorff, Progress and perspectives of electrochemical CO_2 reduction on copper in aqueous electrolyte, *Chem. Rev.*, 2019, **119**, 7610–7672.

21 F. Pan and Y. Yang, Designing CO_2 reduction electrode materials by morphology and interface engineering, *Energy Environ. Sci.*, 2020, **13**, 2275–2309.

22 L. R. L. Ting and B. S. Yeo, Recent advances in understanding mechanisms for the electrochemical reduction of carbon dioxide, *Curr. Opin. Electrochem.*, 2018, **8**, 126–134.

23 M. Li, H. Wang, W. Luo, P. C. Sherrell, J. Chen and J. Yang, Heterogeneous single-atom catalysts for electrochemical CO_2 reduction reaction, *Adv. Mater.*, 2020, **32**, 2001848.

24 H. Liu, Y. Zhu, J. Ma, Z. Zhang and W. Hu, Recent advances in atomic-level engineering of nanostructured catalysts for electrochemical CO_2 reduction, *Adv. Funct. Mater.*, 2020, **30**, 1910534.

25 K. Jiang, S. Siahrostami, A. J. Akey, Y. Li, Z. Lu, J. Lattimer, Y. Hu, C. Stokes, M. Gangishetty, G. Chen, Y. Zhou, W. Hill, W.-B. Cai, D. Bell, K. Chan, J. K. Nørskov, Y. Cui and H. Wang, Transition-metal single atoms in a graphene shell as active centers for highly efficient artificial photosynthesis, *Chem*, 2017, **3**, 950–960.

26 A. Wang, J. Li and T. Zhang, Heterogeneous single-atom catalysis, *Nat. Rev. Chem.*, 2018, **2**, 65–81.

27 U. I. Kramm, J. Herranz, N. Larouche, T. M. Arruda, M. Lefèvre, F. Jaouen, P. Bogdanoff, S. Fiechter, I. Abs-Wurmbach, S. Mukerjee and J.-P. Dodelet, Structure of the catalytic sites in Fe/N/C-catalysts for O_2-reduction in pem fuel cells, *Phys. Chem. Chem. Phys.*, 2012, **14**, 11673–11688.

28 U. Tylus, Q. Jia, K. Strickland, N. Ramaswamy, A. Serov, P. Atanassov and S. Mukerjee, Elucidating oxygen reduction active sites in pyrolyzed metal–nitrogen coordinated non-precious-metal electrocatalyst systems, *J. Phys. Chem. C*, 2014, **118**, 8999–9008.

29 A. Zitolo, V. Goellner, V. Armel, M.-T. Sougrati, T. Mineva, L. Stievano, E. Fonda and F. Jaouen, Identification of catalytic sites for oxygen reduction in iron- and nitrogen-doped graphene materials, *Nat. Mater.*, 2015, **14**, 937–942.

30 D. M. Koshy, A. T. Landers, D. A. Cullen, A. V. Ievlev, H. M. Meyer Iii, C. Hahn, Z. Bao and T. F. Jaramillo, Direct characterization of atomically dispersed catalysts: Nitrogen-coordinated Ni sites in carbon-based materials for CO_2 electroreduction, *Adv. Energy Mater.*, 2020, **10**, 2001836.

31 D. M. Koshy, S. Chen, D. U. Lee, M. B. Stevens, A. M. Abdellah, S. M. Dull, G. Chen, D. Nordlund, A. Gallo, C. Hahn, D. C. Higgins, Z. Bao and T. F. Jaramillo, Understanding the origin of highly selective CO_2 electroreduction to CO on Ni,N-doped carbon catalysts, *Angew. Chem., Int. Ed.*, 2020, **59**, 4043–4050.

32 C. Zhang, L. Shahcheraghi, F. Ismail, H. Eraky, H. Yuan, A. P. Hitchcock and D. Higgins, Chemical structure and distribution in nickel–nitrogen–carbon catalysts for CO_2

electroreduction identified by scanning transmission x-ray microscopy, *ACS Catal.*, 2022, **12**, 8746–8760.

33 R. M. Arán-Ais, D. Gao and B. Roldan Cuenya, Structure- and electrolyte-sensitivity in CO_2 electroreduction, *Acc. Chem. Res.*, 2018, **51**, 2906–2917.

34 W. Ju, A. Bagger, G.-P. Hao, A. S. Varela, I. Sinev, V. Bon, B. Roldan Cuenya, S. Kaskel, J. Rossmeisl and P. Strasser, Understanding activity and selectivity of metal-nitrogen-doped carbon catalysts for electrochemical reduction of CO_2, *Nat. Commun.*, 2017, **8**, 944.

35 P. Su, K. Iwase, S. Nakanishi, K. Hashimoto and K. Kamiya, Nickel-nitrogen-modified graphene: An efficient electrocatalyst for the reduction of carbon dioxide to carbon monoxide, *Small*, 2016, **12**, 6083–6089.

36 K. Jiang, S. Siahrostami, T. Zheng, Y. Hu, S. Hwang, E. Stavitski, Y. Peng, J. Dynes, M. Gangisetty, D. Su, K. Attenkofer and H. Wang, Isolated Ni single atoms in graphene nanosheets for high-performance CO_2 reduction, *Energy Environ. Sci.*, 2018, **11**, 893–903.

37 H. Wang, G. Liu, C. Chen, W. Tu, Y. Lu, S. Wu, D. O'Hare and R. Xu, Single-Ni sites embedded in multilayer nitrogen-doped graphene derived from amino-functionalized MOF for highly selective CO_2 electroreduction, *ACS Sustainable Chem. Eng.*, 2021, **9**, 3792–3801.

38 W. Zheng, C. Guo, J. Yang, F. He, B. Yang, Z. Li, L. Lei, J. Xiao, G. Wu and Y. Hou, Highly active metallic nickel sites confined in N-doped carbon nanotubes toward significantly enhanced activity of CO_2 electroreduction, *Carbon*, 2019, **150**, 52–59.

39 Y. Cheng, S. Zhao, B. Johannessen, J.-P. Veder, M. Saunders, M. R. Rowles, M. Cheng, C. Liu, M. F. Chisholm, R. De Marco, H.-M. Cheng, S.-Z. Yang and S. P. Jiang, Atomically dispersed transition metals on carbon nanotubes with ultrahigh loading for selective electrochemical carbon dioxide reduction, *Adv. Mater.*, 2018, **30**, 1706287.

40 B. Chen, B. Li, Z. Tian, W. Liu, W. Liu, W. Sun, K. Wang, L. Chen and J. Jiang, Enhancement of mass transfer for facilitating industrial-level CO_2 electroreduction on atomic Ni-N_4 sites, *Adv. Energy Mater.*, 2021, **11**, 2102152.

41 Y. Li, S. L. Zhang, W. Cheng, Y. Chen, D. Luan, S. Gao and X. W. Lou, Loading single-Ni atoms on assembled hollow N-rich carbon plates for efficient CO_2 electroreduction, *Adv. Mater.*, 2022, **34**, 2105204.

42 Y. Li, X. F. Lu, S. Xi, D. Luan, X. Wang and X. W. Lou, Synthesis of N-doped highly graphitic carbon urchin-like hollow structures loaded with single-Ni atoms towards efficient CO_2 electroreduction, *Angew. Chem., Int. Ed.*, 2022, **61**, e202201491.

43 K. Mou, Z. Chen, X. Zhang, M. Jiao, X. Zhang, X. Ge, W. Zhang and L. Liu, Highly efficient electroreduction of CO_2 on nickel single-atom catalysts: Atom trapping and nitrogen anchoring, *Small*, 2019, **15**, 1903668.

44 I. Song, Y. Eom, P. M. Austeria, D. H. Hong, M. Balamurugan, R. Boppella, D. H. Kim and T. K. Kim, Geometric and electronic structural engineering of isolated Ni single atoms for a highly efficient CO_2 electroreduction, *Small*, 2023, **19**, 2300049.

45 Y. Li, N. M. Adli, W. Shan, M. Wang, M. J. Zachman, S. Hwang, H. Tabassum, S. Karakalos, Z. Feng, G. Wang, Y. C. Li and G. Wu, Atomically dispersed single Ni site catalysts for high-efficiency CO_2 electroreduction at industrial-level current densities, *Energy Environ. Sci.*, 2022, **15**, 2108–2119.

46 C. Jia, S. Li, Y. Zhao, R. K. Hocking, W. Ren, X. Chen, Z. Su, W. Yang, Y. Wang, S. Zheng, F. Pan and C. Zhao, Nitrogen vacancy induced coordinative reconstruction of single-atom Ni catalyst for efficient electrochemical CO_2 reduction, *Adv. Funct. Mater.*, 2021, **31**, 2107072.

47 C. Jia, X. Tan, Y. Zhao, W. Ren, Y. Li, Z. Su, S. C. Smith and C. Zhao, Sulfur-dopant-promoted electroreduction of CO_2 over coordinatively unsaturated Ni-N_2 moieties, *Angew. Chem., Int. Ed.*, 2021, **60**, 23342–23348.

48 X. Wang, Y. Wang, X. Sang, W. Zheng, S. Zhang, L. Shuai, B. Yang, Z. Li, J. Chen, L. Lei, N. M. Adli, M. K. H. Leung, M. Qiu, G. Wu and Y. Hou, Dynamic activation of adsorbed intermediates via axial traction for the promoted electrochemical CO_2 reduction, *Angew. Chem., Int. Ed.*, 2021, **60**, 4192–4198.

49 M. Huang, B. Deng, X. Zhao, Z. Zhang, F. Li, K. Li, Z. Cui, L. Kong, J. Lu, F. Dong, L. Zhang and P. Chen, Template-sacrificing synthesis of well-defined asymmetrically coordinated single-atom catalysts for highly efficient CO_2 electrocatalytic reduction, *ACS Nano*, 2022, **16**, 2110–2119.

50 W. Ren, X. Tan, W. Yang, C. Jia, S. Xu, K. Wang, S. C. Smith and C. Zhao, Isolated diatomic Ni-Fe metal–nitrogen sites for synergistic electroreduction of CO_2, *Angew. Chem., Int. Ed.*, 2019, **58**, 6972–6976.

51 J. Zhu, M. Xiao, D. Ren, R. Gao, X. Liu, Z. Zhang, D. Luo, W. Xing, D. Su, A. Yu and Z. Chen, Quasi-covalently coupled Ni–Cu atomic pair for synergistic electroreduction of CO_2, *J. Am. Chem. Soc.*, 2022, **144**, 9661–9671.

52 W. Zheng, Y. Wang, L. Shuai, X. Wang, F. He, C. Lei, Z. Li, B. Yang, L. Lei, C. Yuan, M. Qiu, Y. Hou and X. Feng, Highly boosted reaction kinetics in carbon dioxide electroreduction by surface-introduced electronegative dopants, *Adv. Funct. Mater.*, 2021, **31**, 2008146.

53 Q. Wang, K. Liu, K. Hu, C. Cai, H. Li, H. Li, M. Herran, Y.-R. Lu, T.-S. Chan, C. Ma, J. Fu, S. Zhang, Y. Liang, E. Cortés and M. Liu, Attenuating metal-substrate conjugation in atomically dispersed nickel catalysts for electroreduction of CO_2 to CO, *Nat. Commun.*, 2022, **13**, 6082.

54 S. Liang, Q. Jiang, Q. Wang and Y. Liu, Revealing the real role of nickel decorated nitrogen-doped carbon catalysts for electrochemical reduction of CO_2 to CO, *Adv. Energy Mater.*, 2021, **11**, 2101477.

55 F. Wang, G. Wang, P. Deng, Y. Chen, J. Li, D. Wu, Z. Wang, C. Wang, Y. Hua and X. Tian, Ultrathin nitrogen-doped carbon encapsulated Ni nanoparticles for highly efficient electrochemical CO_2 reduction and aqueous Zn- CO_2 batteries, *Small*, 2023, **19**, 2301128.

56 C. F. Wen, F. Mao, Y. Liu, X. Y. Zhang, H. Q. Fu, L. R. Zheng, P. F. Liu and H. G. Yang, Nitrogen-stabilized low-valent Ni motifs for efficient CO_2 electrocatalysis, *ACS Catal.*, 2020, **10**, 1086–1093.

57 S. Bai, L. Tan, C. Ning, G. Liu, Z. Wu, T. Shen, L. Zheng and Y.-F. Song, Revealing the kinetic balance between proton-feeding and hydrogenation in CO_2 electroreduction, *Small*, 2023, **19**, 2300581.

58 H. Li, K. Gan, R. Li, H. Huang, J. Niu, Z. Chen, J. Zhou, Y. Yu, J. Qiu and X. He, Highly dispersed NiO clusters induced electron delocalization of Ni-N-C catalysts for enhanced CO_2 electroreduction, *Adv. Funct. Mater.*, 2023, **33**, 2208622.

59 T. N. Nguyen, M. Salehi, Q. V. Le, A. Seifitokaldani and C. T. Dinh, Fundamentals of electrochemical CO_2 reduction on single-metal-atom catalysts, *ACS Catal.*, 2020, **10**, 10068–10095.

60 T. Wang, J. Wang, C. Lu, K. Jiang, S. Yang, Z. Ren, J. Zhang, X. Liu, L. Chen, X. Zhuang and J. Fu, Single-atom anchored curved carbon surface for efficient CO_2 electro-reduction with nearly 100% CO selectivity and industrially-relevant current density, *Adv. Mater.*, 2023, **35**, 2205553.

61 F. Yu, H. Zhou, Z. Zhu, J. Sun, R. He, J. Bao, S. Chen and Z. Ren, Three-dimensional nanoporous iron nitride film as an efficient electrocatalyst for water oxidation, *ACS Catal.*, 2017, **7**, 2052–2057.

62 H. Kim, D. Shin, W. Yang, D. H. Won, H.-S. Oh, M. W. Chung, D. Jeong, S. H. Kim, K. H. Chae, J. Y. Ryu, J. Lee, S. J. Cho, J. Seo, H. Kim and C. H. Choi, Identification of single-atom Ni site active toward electrochemical CO_2 conversion to CO, *J. Am. Chem. Soc.*, 2021, **143**, 925–933.

63 C. J. Ballhausen and M. A. Weiner, Introduction to ligand field theory, *J. Electrochem. Soc.*, 1963, **110**, 97Cb.

64 M. Ma, F. Li and Q. Tang, Coordination environment engineering on nickel single-atom catalysts for CO_2 electroreduction, *Nanoscale*, 2021, **13**, 19133–19143.

65 C. Hu, Y. Wang, J. Chen, H.-F. Wang, K. Shen, K. Tang, L. Chen and Y. Li, Main-group metal single-atomic regulators in dual-metal catalysts for enhanced electrochemical CO_2 reduction, *Small*, 2022, **18**, 2201391.

66 H. B. Yang, S.-F. Hung, S. Liu, K. Yuan, S. Miao, L. Zhang, X. Huang, H.-Y. Wang, W. Cai, R. Chen, J. Gao, X. Yang, W. Chen, Y. Huang, H. M. Chen, C. M. Li, T. Zhang and B. Liu, Atomically dispersed Ni(i) as the active site for electrochemical CO_2 reduction, *Nat. Energy*, 2018, **3**, 140–147.

67 S. Schnur and A. Groß, Strain and coordination effects in the adsorption properties of early transition metals: A density-functional theory study, *Phys. Rev. B: Condens. Matter Mater. Phys.*, 2010, **81**, 033402.

68 X. Li, Y. Zeng, C.-W. Tung, Y.-R. Lu, S. Baskaran, S.-F. Hung, S. Wang, C.-Q. Xu, J. Wang, T.-S. Chan, H. M. Chen, J. Jiang, Q. Yu, Y. Huang, J. Li, T. Zhang and B. Liu, Unveiling the in situ generation of a monovalent Fe(i) site in the single-Fe-atom catalyst for electrochemical CO_2 reduction, *ACS Catal.*, 2021, **11**, 7292–7301.

69 W. Liu, L. Zhang, X. Liu, X. Liu, X. Yang, S. Miao, W. Wang, A. Wang and T. Zhang, Discriminating catalytically active FeN_x species of atomically dispersed Fe-N-C catalyst for selective oxidation of the C-H bond, *J. Am. Chem. Soc.*, 2017, **139**, 10790–10798.

70 W. Liu, Y. Chen, H. Qi, L. Zhang, W. Yan, X. Liu, X. Yang, S. Miao, W. Wang, C. Liu, A. Wang, J. Li and T. Zhang, A durable nickel single-atom catalyst for hydrogenation reactions and cellulose valorization under harsh conditions, *Angew. Chem., Int. Ed.*, 2018, **57**, 7071–7075.

71 J. Luo, G. I. N. Waterhouse, L. Peng and Q. Chen, Recent progress in high-loading single-atom catalysts and their applications, *Ind. Chem. Mater.*, 2023, **1**, 486–500.

72 J. Li, A. Zitolo, F. A. Garcés-Pineda, T. Asset, M. Kodali, P. Tang, J. Arbiol, J. R. Galán-Mascarós, P. Atanassov, I. V. Zenyuk, M. T. Sougrati and F. Jaouen, Metal oxide clusters on nitrogen-doped carbon are highly selective for CO_2 electroreduction to CO, *ACS Catal.*, 2021, **11**, 10028–10042.

73 Y. Cao, S. Chen, S. Bo, W. Fan, J. Li, C. Jia, Z. Zhou, Q. Liu, L. Zheng and F. Zhang, Single atom Bi decorated copper alloy enables C-C coupling for electrocatalytic reduction of CO_2 into C_{2+} products, *Angew. Chem., Int. Ed.*, 2023, **62**, e202303048.

74 Z. Li, J. Jiang, X. Liu, Z. Zhu, J. Wang, Q. He, Q. Kong, X. Niu, J. S. Chen, J. Wang and R. Wu, Coupling atomically dispersed $Fe\text{-}N_5$ sites with defective N-doped carbon boosts CO_2 electroreduction, *Small*, 2022, **18**, 2203495.

75 Y. Pan, R. Lin, Y. Chen, S. Liu, W. Zhu, X. Cao, W. Chen, K. Wu, W.-C. Cheong, Y. Wang, L. Zheng, J. Luo, Y. Lin, Y. Liu, C. Liu, J. Li, Q. Lu, X. Chen, D. Wang, Q. Peng, C. Chen and Y. Li, Design of single-atom $Co\text{-}N_5$ catalytic site: A robust electrocatalyst for CO_2 reduction with nearly 100% co selectivity and remarkable stability, *J. Am. Chem. Soc.*, 2018, **140**, 4218–4221.

76 L. Wang, X. Lai, Y. Xu, S. Luo, L. Wang, K. Yan, D. Zhang, S. Feng and Y. Xu, Fabricating penta-coordinated Fe single atoms for electrochemical CO_2 reduction to syngas, *Catal. Sci. Technol.*, 2023, **13**, 3946–3952.

77 C. Xiao, L. Cheng, Y. Zhu, G. Wang, L. Chen, Y. Wang, R. Chen, Y. Li and C. Li, Super-coordinated nickel $N_4Ni_1O_2$ site single-atom catalyst for selective H_2O_2 electrosynthesis at high current densities, *Angew. Chem., Int. Ed.*, 2022, **61**, e202206544.

78 Y. Li, F. Li, A. Laaksonen, C. Wang, P. Cobden, P. Boden, Y. Liu, X. Zhang and X. Ji, Electrochemical CO_2 reduction with ionic liquids: review and evaluation, *Ind. Chem. Mater.*, 2023, **1**, 410–430.